Supplementary Information for:

MamY is a membrane-bound protein that aligns magnetosomes and the motility axis of helical magnetotactic bacteria

Toro-Nahuelpan, M.[1,2,3], G. Giacomelli[4], O. Raschdorf[1,2,5], S. Borg[1,6], J.M. Plitzko[2], M. Bramkamp[4], D. Schüler[1] and F.D. Müller[1]*.

[1]Department of Microbiology, University of Bayreuth, Bayreuth, Germany.
[2]Department of Molecular Structural Biology, Max Planck Institute of Biochemistry, Planegg-Martinsried, Germany.
[3]Present address: European Molecular Biology Laboratory, Heidelberg, Germany.
[4]Department of Biology I, Ludwig-Maximilian-University Munich, Planegg-Martinsried, Germany.
[5]Present address: Thermo Fisher Scientific (formerly FEI Company), Eindhoven, The Netherlands.
[6]Present address: Bundeswehr Institute of Microbiology, Bundeswehr, Munich, Germany.

*Corresponding author and lead contact:
Dr. Frank D. Müller
Department of Microbiology, University of Bayreuth, 95447 Bayreuth, Germany.
E-mail: frank.mueller@uni-bayreuth.de

Contents:

Supplementary Figures

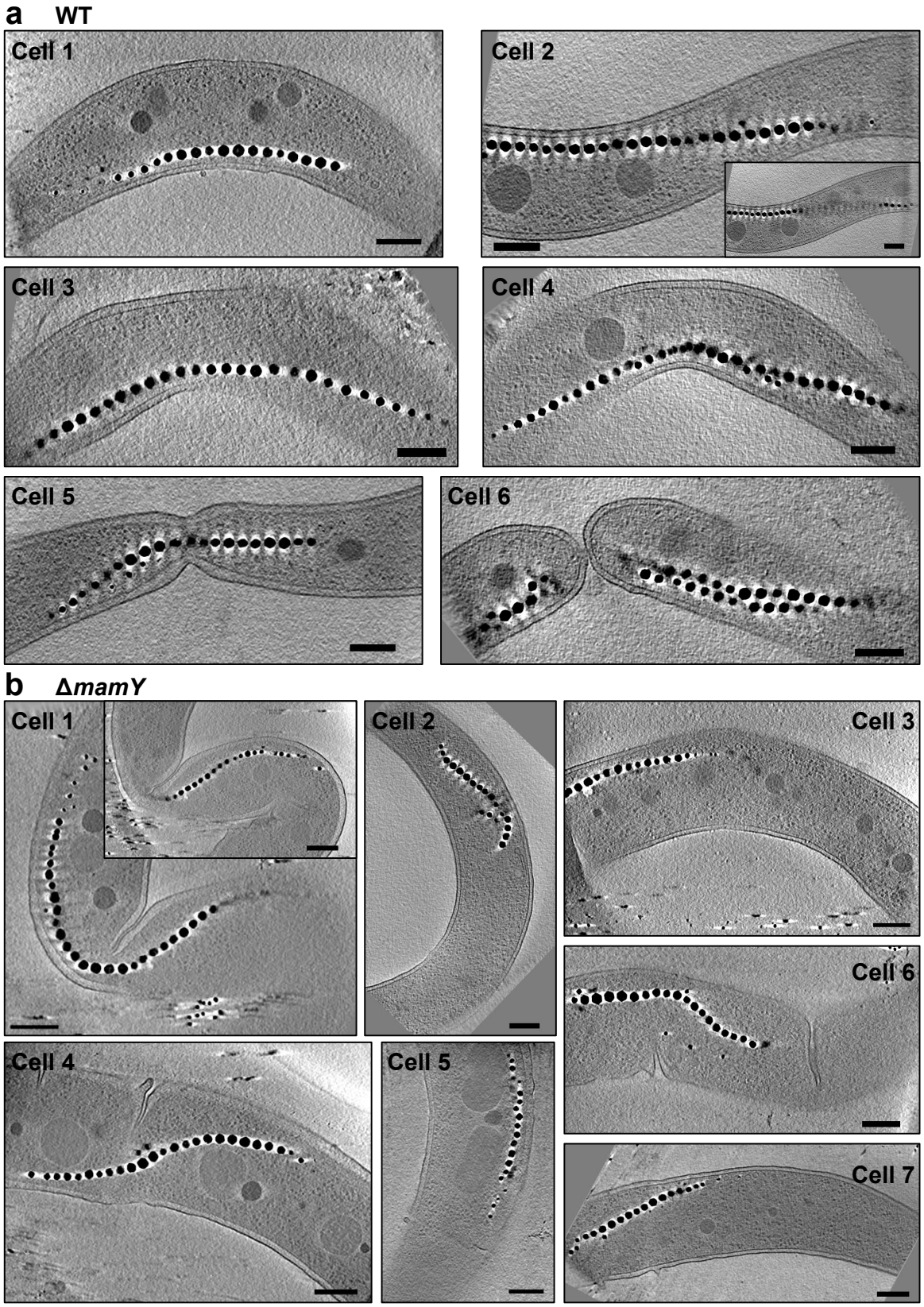

Supplementary Figure 1. Cryo-ET of WT and Δ*mamY* strains.

Cryo-ET tomographic slices of several **(a)** WT (n=7) and **(b)** Δ*mamY* (n=9) cells showing the intracellular magnetosome chain localization. Slice thickness: 15.7 nm. Scale bars: 200 nm.

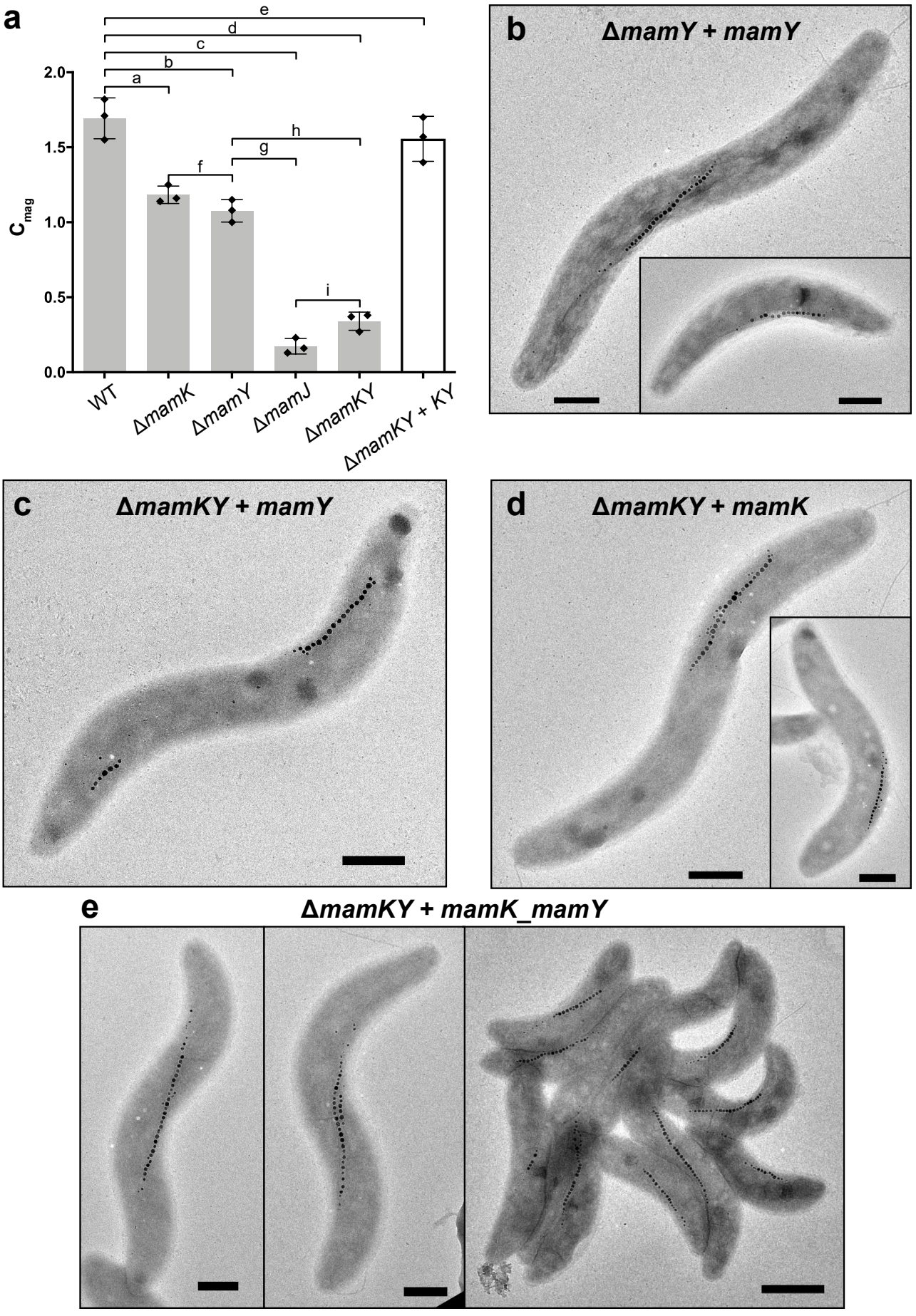
a
b
ΔmamY + mamY
c
ΔmamKY + mamY
d
ΔmamKY + mamK
e
ΔmamKY + mamK_mamY
C_{mag}
2.0
1.5
1.0
0.5
0.0
a
b
c
d
e
f
g
h
i
WT
ΔmamK
ΔmamY
ΔmamJ
ΔmamKY
ΔmamKY + KY

Supplementary Figure 2. Magnetic response and mutant complementation assays

(a) Magnetic response (C_{mag}) of fixed cells from the WT, Δ*mamK,* Δ*mamY,* Δ*mamJ* and Δ*mamKY* strains. The values are derived from four independent samples (n=4) for each strain. A one-way ANOVA and a post hoc Tukey's multiple comparison test resulted in the differences shown in the plot. The test shows that Δ*mamJ* vs Δ*mamKY* strains as well as Δ*mamK* vs Δ*mamY* do not differ significantly in C_{mag}, but all of them are different from the WT (P values: a = 0.00003214; b = 0.00000496; c and d represent a *P value* < 0.00000001; e = 0.11009048 (ns); f = 0.20297774 (ns); g = 0.00000009; h = 0.00000078; i = 0.05712370 (ns)). ns: not significant. Error bars represent the SD. The centre represent the mean. Individual data points (diamonds) per strain are overlaid on the bar to indicate the distribution of the data set.

(b) TEM micrograph of Δ*mamY* cells complemented with the *mamY* gene.

(c) TEM micrograph of Δ*mamKY* cells complemented with *mamY*, **(d)** *mamK* and **(e)** *mamK-mamY* genes. Similar magnetosome localization patterns as shown in (b-e) were observed in cells of at least three independent experiments. Scale bars: 500 nm (except most right micrograph in E: 1 μm).

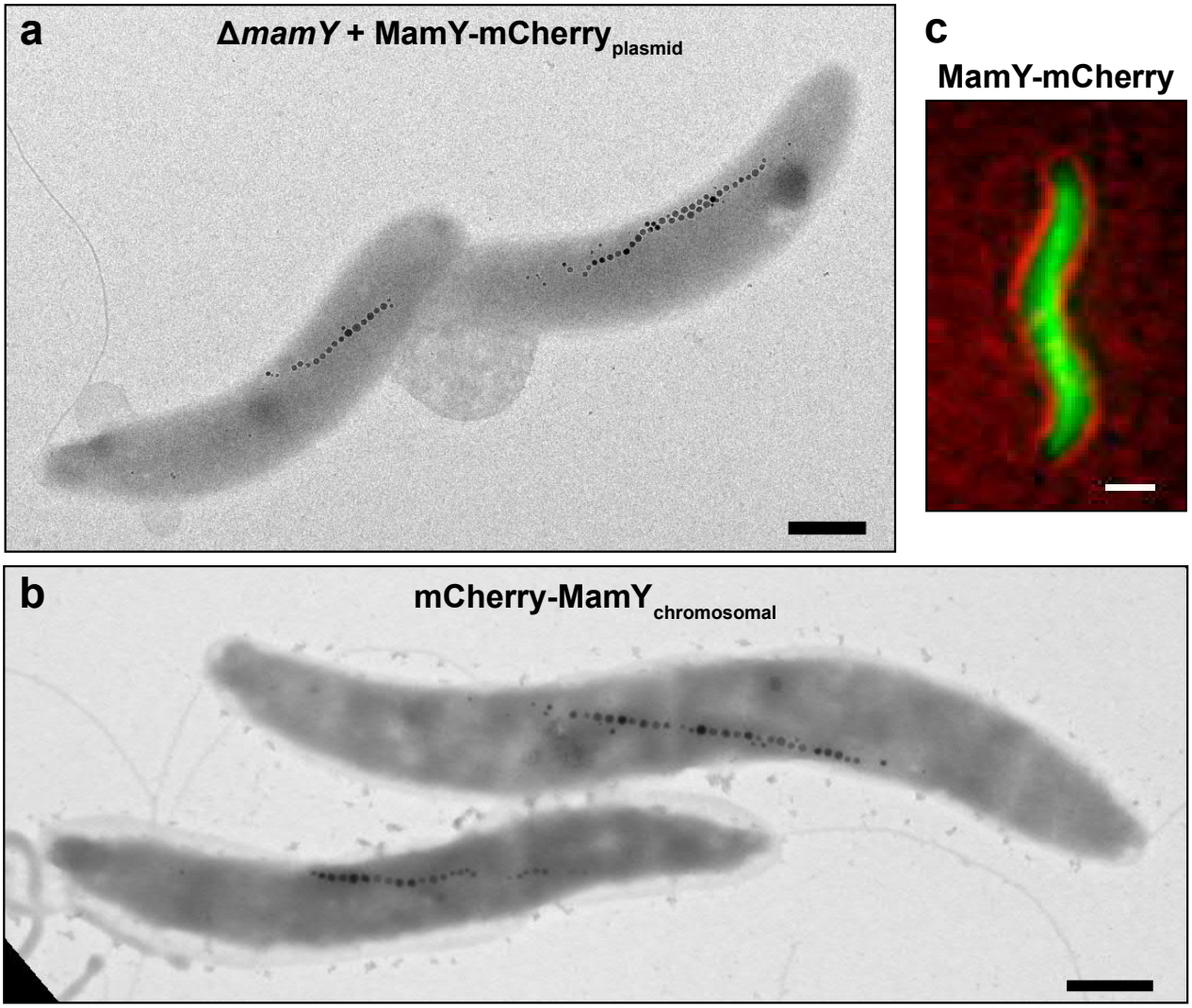

Supplementary Figure 3. N- and C-terminally tagged MamY proteins are functional

(a) TEM micrograph of the Δ*mamY* strain complemented with *mamY-mCherry* showing that the C-terminal tagged MamY restores the WT magnetosome chain positioning and thereby is functional.

(b) TEM micrograph of a markerless native site in-frame chromosomally inserted *mCherry* gene upstream of *mamY* resulting in the *mCherry-mamY* fusion. This N-terminally tagged MamY shows a WT magnetosome chain positioning phenotype, demonstrating functionality. Scale bars of TEM micrographs: 500 nm.

(c) Fluorescence image of a C-terminal mCherry fusion to MamY displaying a linear localization along the positive curvature *of Mgryph*. Scale bar: 1 µm. The magnetosome and mCherry-MamY localization patterns shown could be reproduced in cells of three experiments using independent mutant strains and cell preparations.

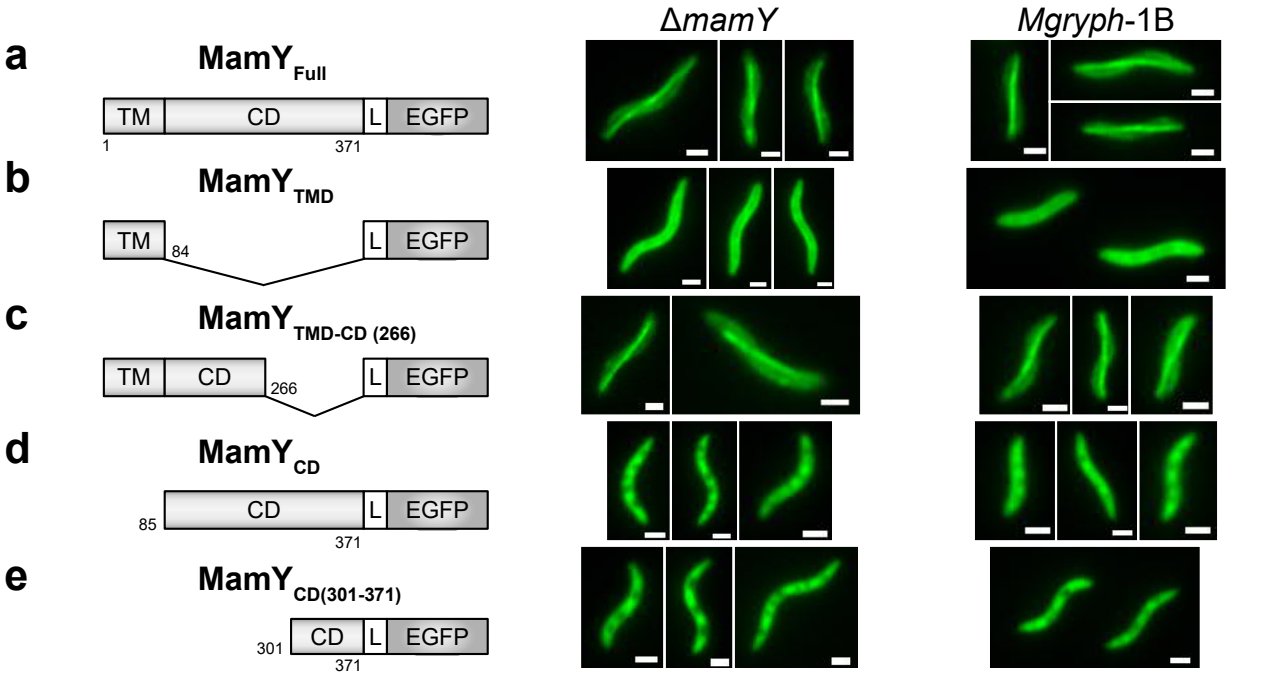
a
MamY Full
TM
CD
L
EGFP
1
371
b
MamY TMD
84
c
MamY TMD-CD (266)
266
d
MamY CD
85
e
MamY CD(301-371)
301
ΔmamY
Mgryph-1B

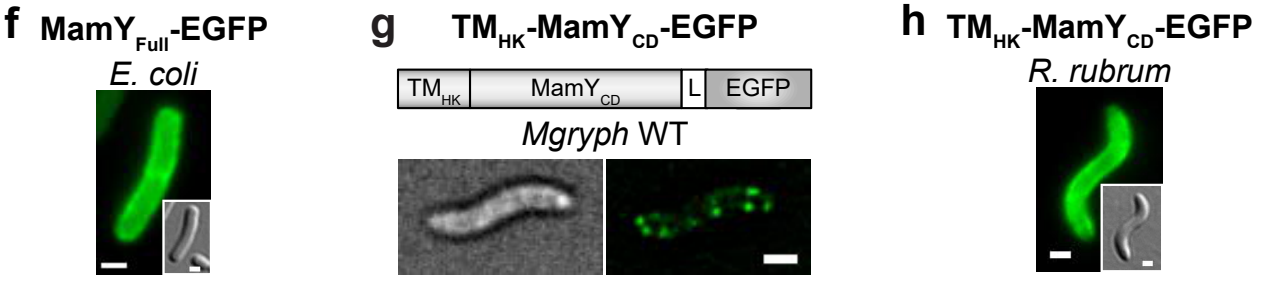
f MamY Full-EGFP
E. coli
g TMHK-MamYCD-EGFP
TMHK
MamYCD
L
EGFP
Mgryph WT
h TMHK-MamYCD-EGFP
R. rubrum

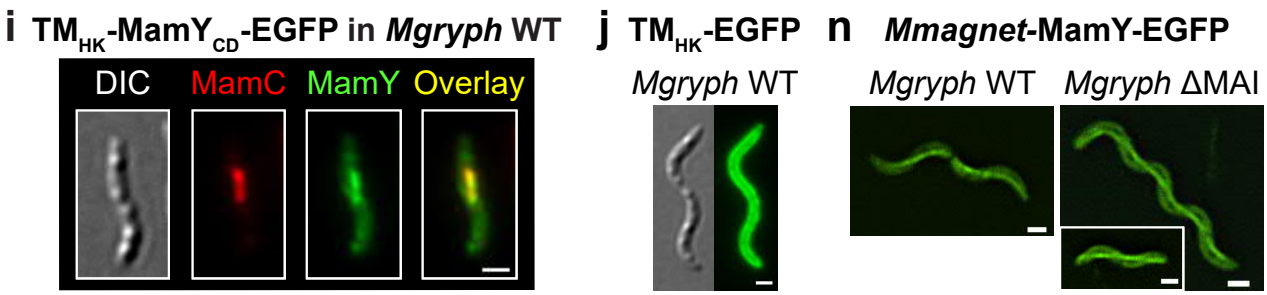
i TMHK-MamYCD-EGFP in Mgryph WT
DIC
MamC
MamY
Overlay
j TMHK-EGFP
Mgryph WT
n Mmagnet-MamY-EGFP
Mgryph WT
Mgryph ΔMAI

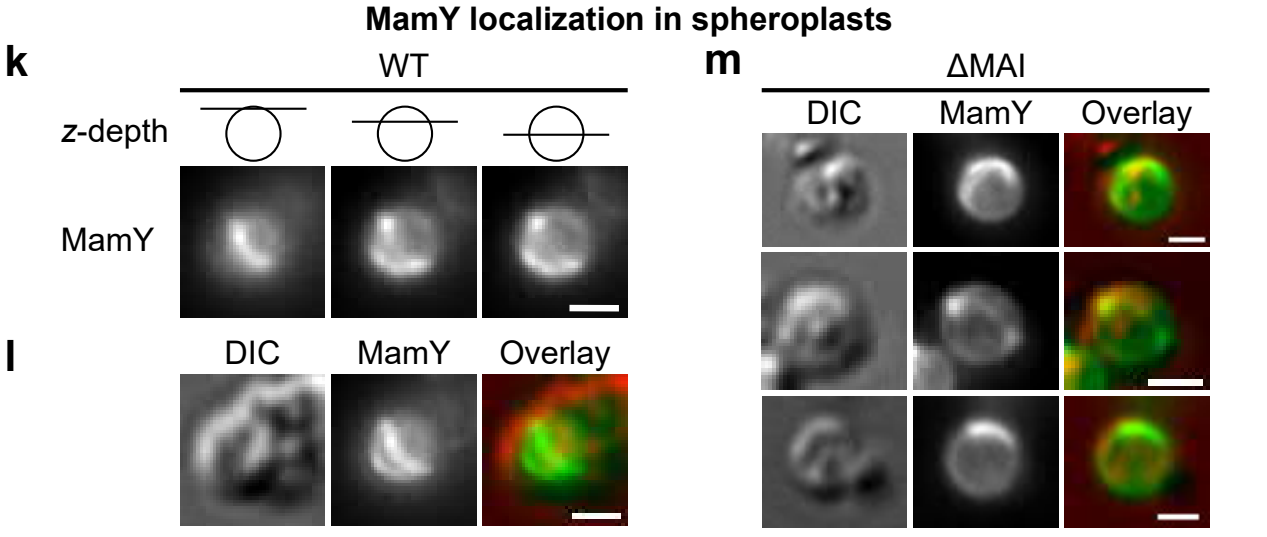
MamY localization in spheroplasts
k
WT
z-depth
MamY
l
DIC
MamY
Overlay
m
ΔMAI
DIC
MamY
Overlay

Supplementary Figure 4. MamY truncation analysis and TM domain exchange

(a-e) Localization patterns of EGFP-tagged MamY variants in Δ*mamY* (left panel) and the non-magnetic mutant *Mgryph*-1B (right panel) observed by fluorescence microscopy.

(a) $MamY_{Full}$: consists of a predicted transmembrane (TM) domain plus the cytoplasmic domain (CD).

(b) $MamY_{TMD}$: harbors the TM domain only.

(c) $MamY_{TMD\text{-}CD(266)}$: N-terminal 266 amino acids (including TM domain).

(d) $MamY_{CD}$: cytoplasmic domain only.

(e) $MamY_{CD(301\text{-}371)}$: C-terminal 71 amino acids only.

(f) $MamY_{Full}$-EGFP localizes to the membrane in the rod-shaped *E. coli*.

(g) MamY TM domain exchanged against a histidine kinase TM domain (TM_{HK}-$MamY_{CD}$). Subcellular localization in the non-magnetic *Mgryph*-1B (central slice through the cell of a deconvolved z-stack). Scheme of the protein fusion is not to scale.

(h) TM_{HK}-$MamY_{CD}$ (MamY TM domain exchanged against the TM domain of the histidine kinase (HK) Mgr_1233) in the heterologous host *R. rubrum* displays diffuse localization to the membrane.

(i) TM_{HK}-$MamY_{CD}$-GFP localization in the WT strain.

(j) Localization of the EGFP-tagged TM domain of the histidine kinase (HK) in the *Mgryph* WT.

(k-l) Spheroplasts of WT and ΔMAI strains expressing MamY-EGFP. **(k)** Micrograph slices through a deconvolved z-stack at several depths of a WT cell. **(l)** Maximum intensity projection micrograph of MamY-EGFP signal of a deconvolved z-stack from the cell shown in (k), and the overlay with the DIC channel.

(m) Maximum intensity projection micrographs of MamY-EGFP signal (of a deconvolved z-stack) from three ΔMAI cells and overlay with the DIC channel. All linear structures appear membrane associated, either at the top, bottom or edges of the spheroplasts.

(n) Localization of *Mmagnet*-MamY fused to EGFP in the *Mgryph* WT (left panel) and ΔMAI (right panel, this strain is devoid of magnetosome-related genes by deletion of the genomic magnetosome island). A continuous and linear localization from pole-to-pole and likely along the inner positive curvature is evident in both strains, i.e., even in the absence of native *Mgryph*-MamY or other magnetosome-related proteins.

The localization patterns of MamY variants were observed in cells of four (a-e), five (f, h, j) and three (g, i, k-n) experiments using independent mutant strains and cell preparations. All scale bars in the figure: 1µm.

a **Δ*mamY*, *mamC-mamY*$_{CD}$**

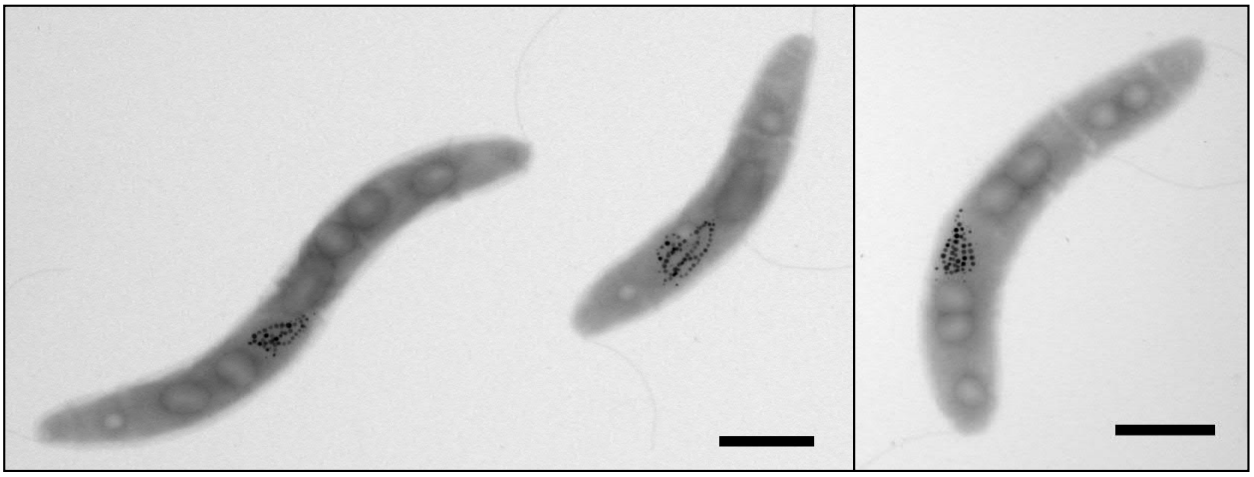

b ***mamC-mamY*$_{CD}$**

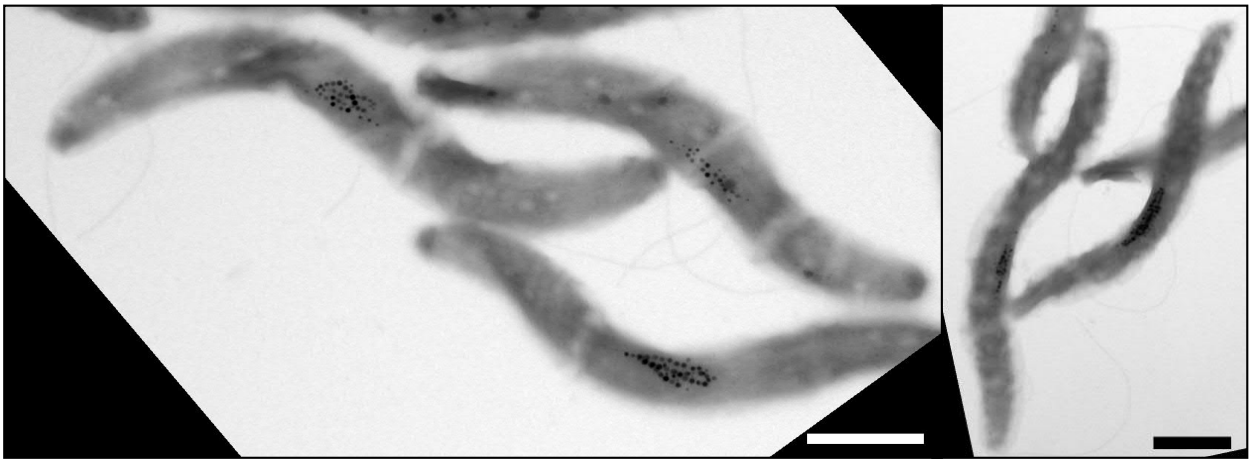

c **MamY:MamC ratio in the magnetosome membrane**

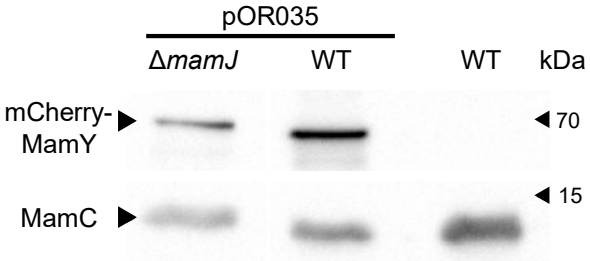

d **BTH of MamY and MamJ**

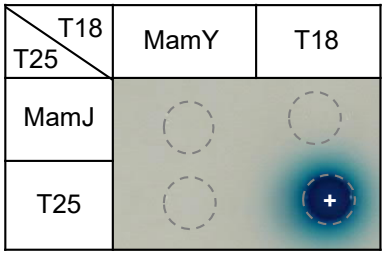

e **BTH of MamY$_{Full}$ and truncated variants**

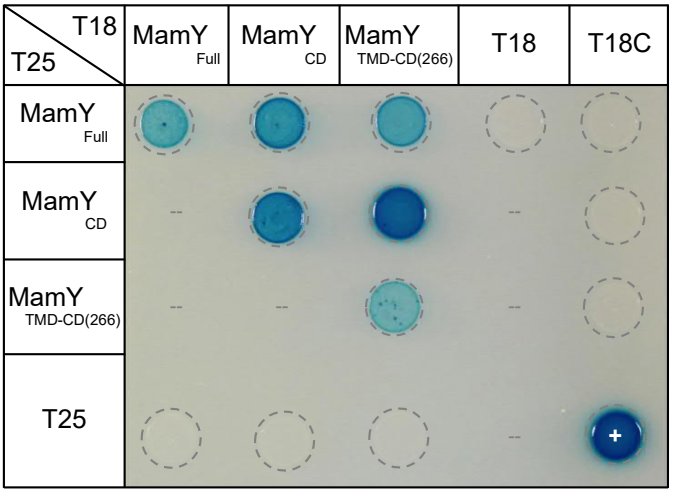

Supplementary Figure 5. Clustered magnetosome phenotype upon exclusive recruitment of MamY $_{CD}$ to the magnetosome membrane by fusion to MamC; reduced MamY content in magnetosomes of the *mamJ* mutant, and *in vivo*-interaction of MamY with MamJ and truncated MamY versions determined by bacterial two-hybrid (BTH) assays

Fusion of the MamY cytoplasmic domain (MamY $_{CD}$) to MamC results in the *mamC-MamY*$_{CD}$ allele at the native *mamC* locus. TEM micrographs of **(a)** Δ*mamY, mamC-mamY*$_{CD}$ and **(b)** *mamC-mamY*$_{CD}$ (in the WT background, native *mamY* present) show aggregated magnetosomes primarily located at the negative or positive curvature, respectively. Similar magnetosome localization patterns were observed in cells of two experiments using independent mutant strains and cell preparations Scale bars: 1 µm.

(c) Simultaneous immunodetection of MamC (as reference) and mCherry-MamY on isolated magnetosomes from WT and the *mamJ* mutant suggests reduced amounts of MamY at Δ *mamJ* magnetosomes (quantified by densitometry, see Methods section). Similar results were obtained from a second experiment using an independent cell sample.

(d) Bacterial two-hybrid analysis of MamJ-MamY interaction. *E. coli* BTH101 was transformed with pairs of plasmids encoding fusions of MamY to the T18 fragment and MamJ to the T25 fragment of *Bordetella pertussis* adenylate cyclase. Positive control (+): T25-zip/T18-zip. An interaction in *E. coli* could not be detected unambiguously.

(e) Detection of MamY self-interaction by bacterial two-hybrid analysis. *E. coli* BTH101 was transformed with pairs of plasmids encoding fusions of MamY to the T25 and T18 fragments. Interaction is evidenced by the growth of blue colonies. Positive control (+): T25-zip/T18-zip. All BTH experiments were repeated at least twice and resulted in similar colony coloring.

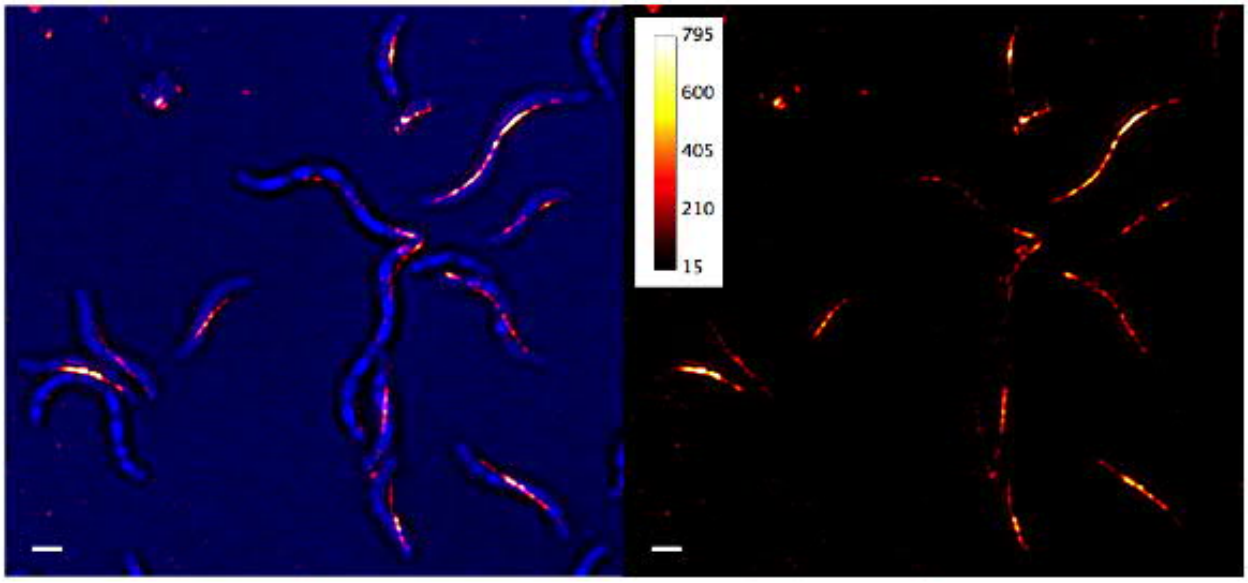

Supplementary Figure 6. 3D-SIM of mCherry-MamY

3D-SIM imaging of cells expressing *mCherry-mamY* from the *mamY* locus. Left panel: Micrograph of a *z*-stack maximum intensity projection of the mCherry-MamY signal combined with brightfield channel. Right panel: mCherry channel only. Similar results were obtained from two independent experiments. Scale bars: 1µm.

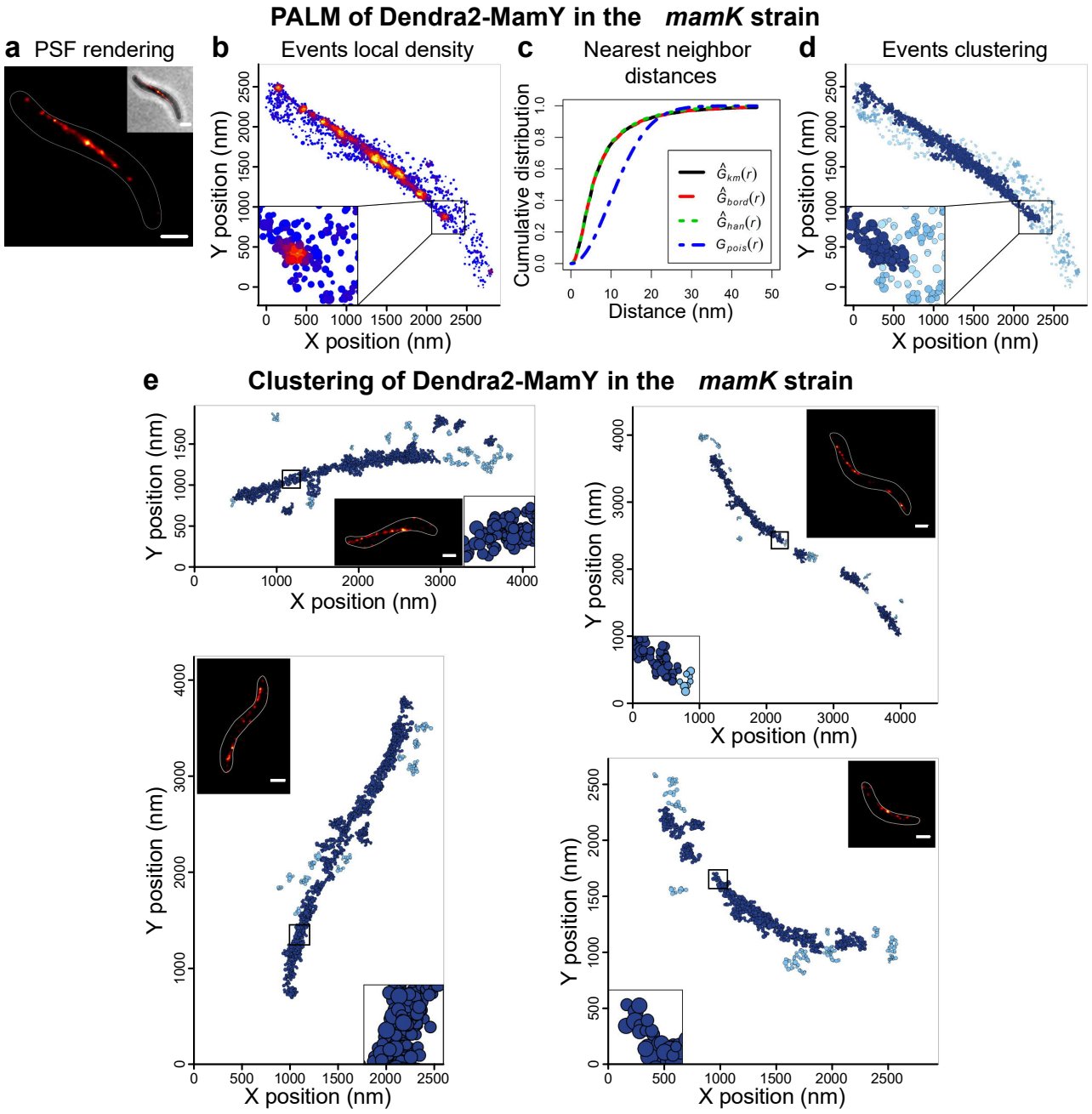

Supplementary Figure 7. PALM of Dendra2-MamY reveals a linear structure along the positive curvature *in vivo* in the absence of MamK

(a-d) Single-molecule detection of Dendra2 fused to MamY in the Δ*mamK* strain (native MamY present).

(a) PSF rendering: a computed fluorescence image generated by density rendering of the PSF FWHM of all detected single events. Insets: brightfield channel. Scale bars: 500 nm.

(b) Local density: each dot represents the geometric center position of a fluorophore. The density of events is depicted in color-coded values (see methods), where the scale values are equivalent to Figure 4e. Lower insets: magnification of the indicated area.

(c) Nearest neighbor distances of the experimental distribution. Data were edge-corrected using three different methods (the border method (red line), Kaplan-Meier (black line) or Hanisch (green line)

estimators) yielding similar results. A theoretical distribution (blue line) represents randomly distributed data considering identical area and amounts of events per cell as the experimental data.

(d) Clustering: algorithm that takes into consideration the localization precision area of individual events and the intermolecular distances. Two molecules are clustered if the distance of their localization precision areas are ≤ 0 nm. Light blue: single molecules and clusters < 5 molecules; Blue: clusters of 5 to 50 molecules; Dark blue: clusters of > 50 molecules. Insets: magnification of the indicated area showing clusters of molecules rendered with their corresponding localization precision area.

(e) PALM imaging of Dendra2-MamY in several Δ*mamK* cells and application of the clustering algorithm. A range of 1,850 to 3,900 single-molecule events per cell with a localization precision average of ~25 nm were acquired. Insets: computed PSF rendering and magnification of the indicated area showing the clusters and molecules rendered with their corresponding localization precision area (Blue: clusters of 5 to 50 molecules; Dark blue: clusters of > 50 molecules). Scale bars: 500 nm. PALM data of Dendra2-MamY in the Δ*mamK* strain (across the figure) are representative of three independent experiments.

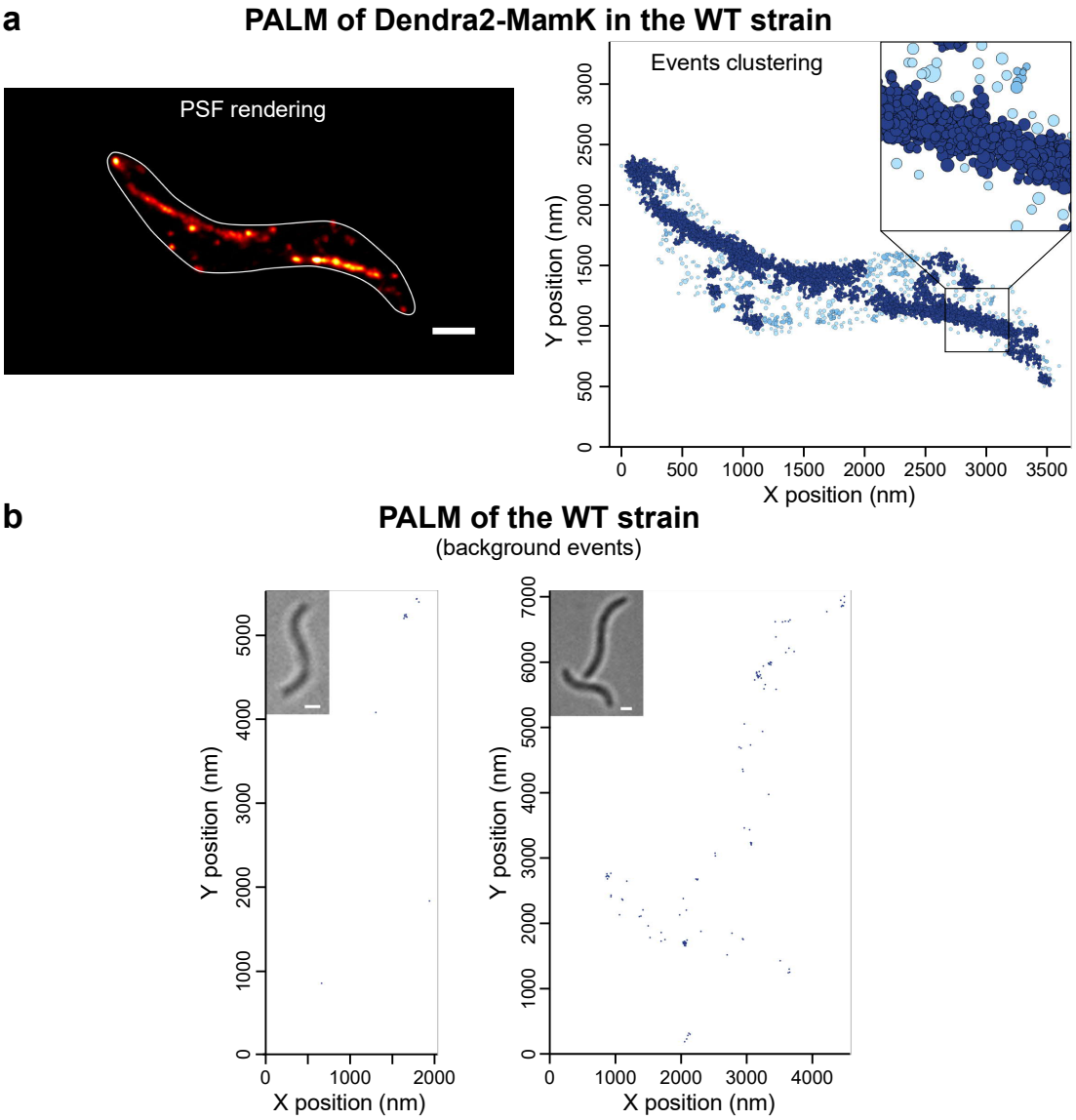

Supplementary Figure 8. Clustering algorithm validation using MamK filaments and and imaging quality assurance: determination of background events in the WT strain.

(a) PALM of Dendra2-MamK in the WT strain as internal control for application of the clustering algorithm to a filament/polymer-forming protein. (Left panel) PSF rendering: a computed fluorescence image generated by density rendering of the PSF FWHM of all detected single events. Scale bar: 500 nm. (Right panel) Events Clustering: algorithm that takes into consideration the localization precision area of individual events and the intermolecular distances. Two molecules are clustered if the distance of their localization precision areas are ≤0 nm. Light blue: single molecules and clusters <5 molecules; Blue: clusters of 5 to 50 molecules; Dark blue: clusters of >50 molecules. Localization precision average of ~26 nm. Insets: magnification of the indicated area showing the clusters and molecules rendered with their corresponding localization precision area. Results are representative of three independent experiments.
(b) WT cells (no fluorophore present) imaged by PALM. Centroids show the background events intrinsic of *Mgryph* cells (average: 82 events/cell, n = 5). Insets: brightfield channel. Scale bars: 500 nm.

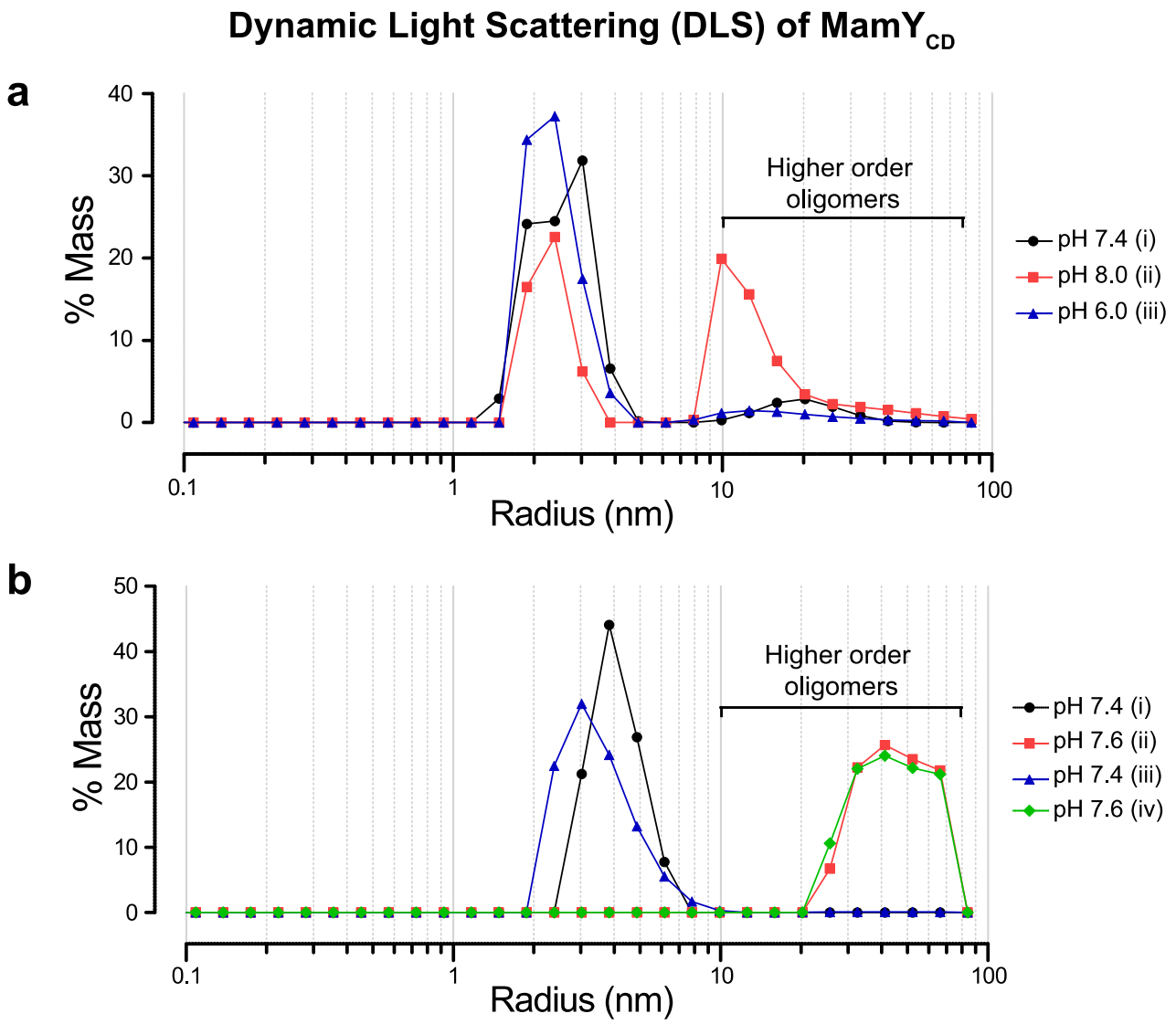

Supplementary Figure 9. The cytoplasmic domain of MamY is able to reversibly self-interact in a pH dependent manner *in vitro*

The purified cytoplasmic domain of MamY (MamY $_{CD}$) was subjected to pH shifts and the dynamic light scattering radius plotted against the total molecules mass. pH changes were as follows:

(a) 7.4 – 8.0 – 6.0; **(b)** 7.4 – 7.6 – 7.4 – 7.6. This experiment was performed independently at least 3 times yielding similar results.

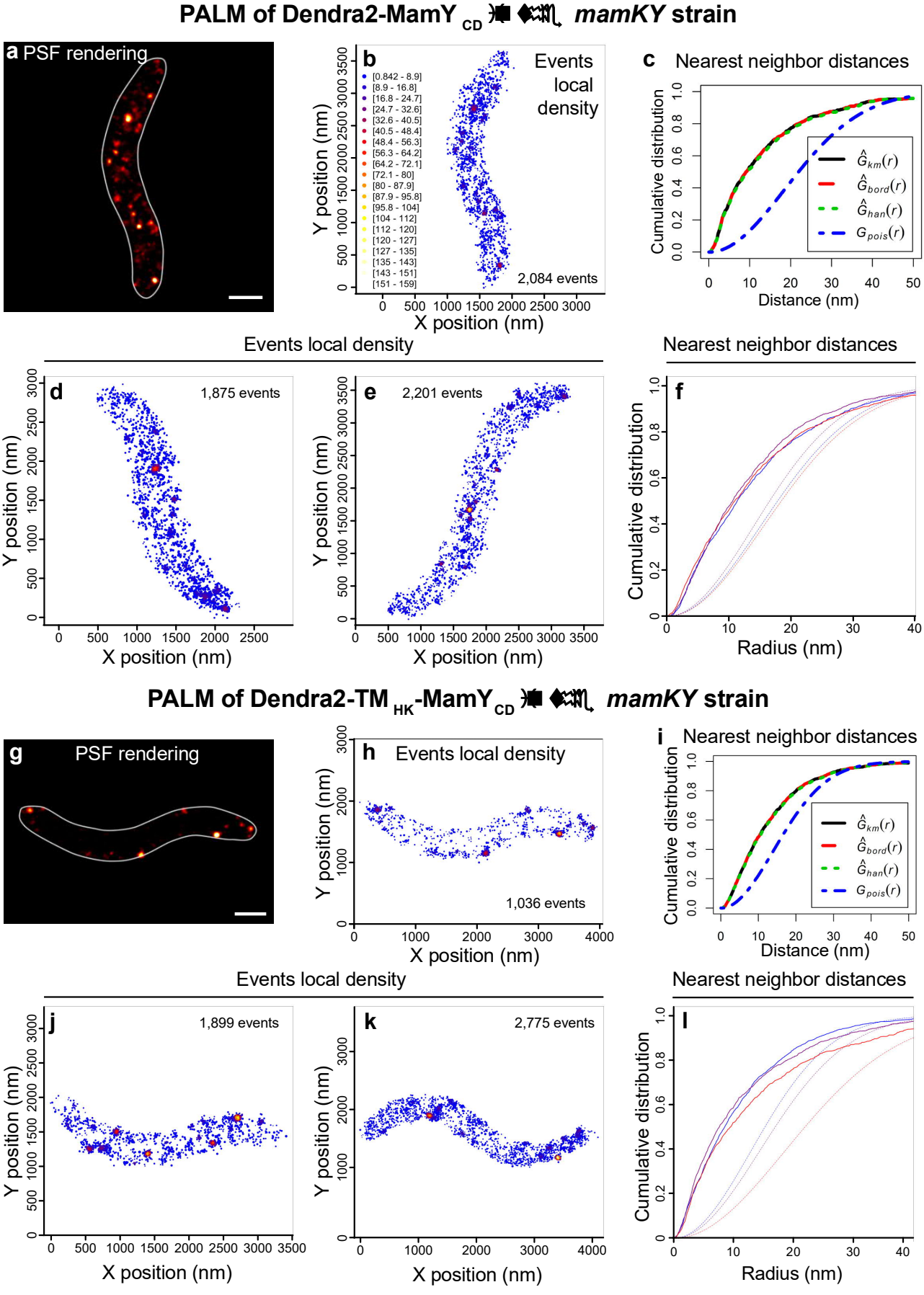
PALM of Dendra2-MamY CD mamKY strain
a PSF rendering
b
Events local density
2,084 events
Y position (nm)
X position (nm)
c Nearest neighbor distances
Cumulative distribution
Distance (nm)
Events local density
Nearest neighbor distances
d 1,875 events
e 2,201 events
f
Radius (nm)
PALM of Dendra2-TM HK-MamY CD mamKY strain
g PSF rendering
h Events local density
1,036 events
i Nearest neighbor distances
Events local density
Nearest neighbor distances
j 1,899 events
k 2,775 events
l

Supplementary Figure 10. PALM of MamY protein variants shows that the transmembrane domain is essential for proper formation of the linear structure

(a-f) PALM of Dendra2 fused to MamY $_{CD}$ protein in the Δ*mamKY* strain. Localization precision average ~25 nm.

(a) PSF rendering: a computed fluorescence image generated by density rendering of the PSF FWHM of all detected single events. Scale bar: 500 nm.

(b, d, e) Local density map of three cells: each dot represents the geometric center position of a fluorophore. The density of events is depicted in color-coded values (see Methods). Scale of values in (b).

(c) Nearest neighbor distances of events of cell shown in (b).

(f) Nearest neighbor distances of all three cells. Blue to red color gradient of the plot lines represent the lowest and highest MamY molecule counts per cell, respectively. Experimental distribution data from three cells was edge-corrected using the Hanisch estimator method (continuous lines). A theoretical distribution -blue line in (c) or dashed lines in (f)- represents randomly distributed data considering identical area and amounts of events per cell as the experimental data. The three depicted and analyzed cells for Dendra2-MamY$_{CD}$ are representative of a single PALM experiment.

(g-l) PALM of Dendra2 fused to the chimeric TM $_{HK}$-MamY$_{CD}$ protein in the Δ*mamKY* strain. Localization precision average ~23 nm.

(g) Computed PSF rendering. Scale bar: 500 nm.

(h, j, k) Local density map: each dot represents the geometric center position of a fluorophore. The density of events is depicted in color-coded values. See scale of values in (b).

(i) Nearest neighbor distances of events of cell shown in (h).

(l) Nearest neighbor distances of all three cells. Blue to red color gradient of the plot lines represent the lowest and highest MamY molecule counts per cell, respectively. Experimental distribution data from three cells was edge-corrected using the Hanisch estimator method (continuous lines). A theoretical distribution -blue line in (i) or dashed lines in (l)- represents randomly distributed data considering identical area and amounts of events per cell as the experimental data. Images for the Dendra2- TM $_{HK}$-MamY$_{CD}$ fusion are representative of two independent experiments.

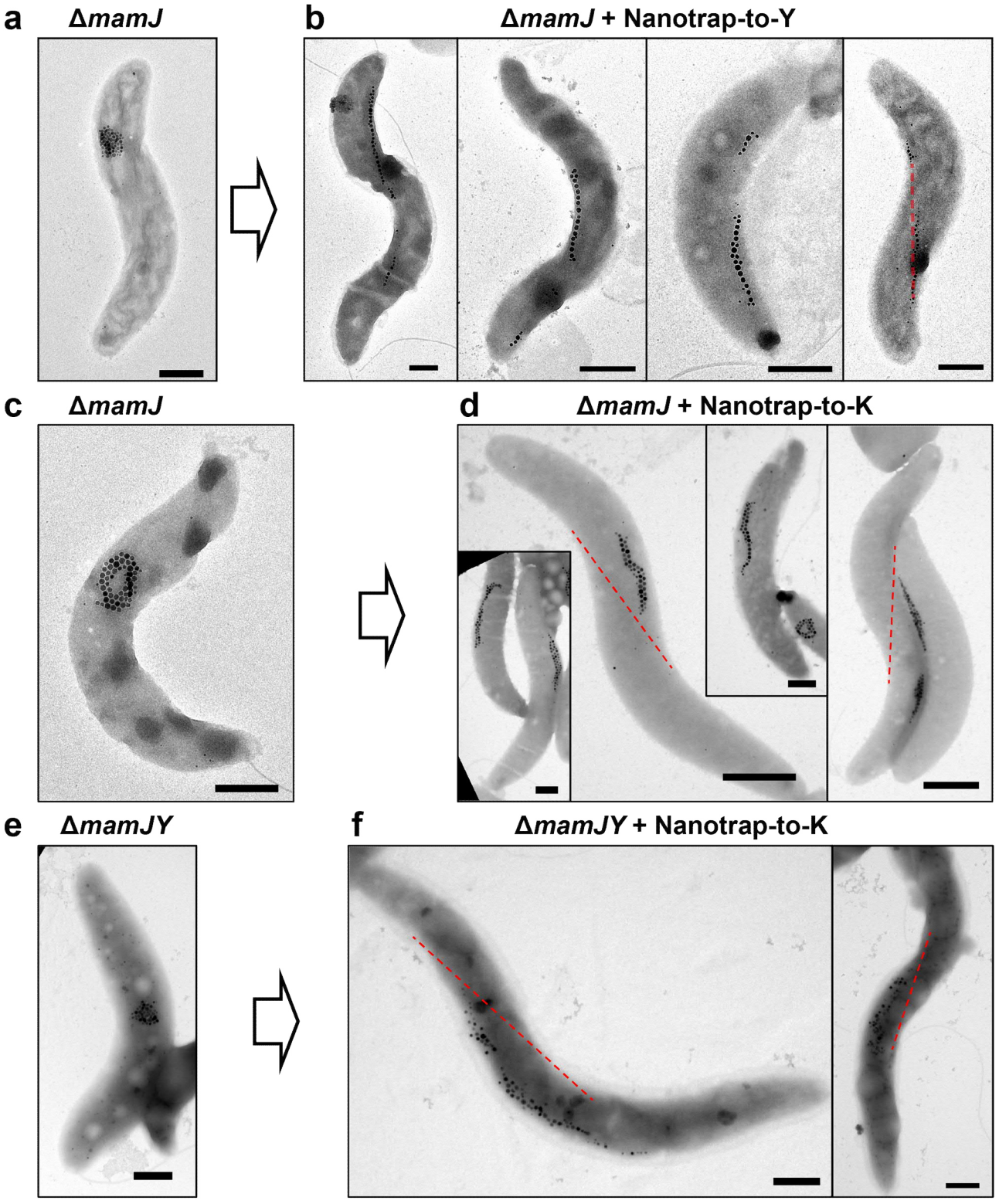
a
ΔmamJ
b
ΔmamJ + Nanotrap-to-Y
c
ΔmamJ
d
ΔmamJ + Nanotrap-to-K
e
ΔmamJY
f
ΔmamJY + Nanotrap-to-K

Supplementary Figure 11. *In vivo*-reconstruction of a synthetic magnetosome chain onto MamY and MamK structures

(a) TEM micrograph of a Δ*mamJ* cell harboring the typical agglomerated magnetosomes. Scale bar: 500 nm.

(b) Δ*mamJ* cells expressing the Nanotrap-to-Y (mCherry-MamY and MamC-MBN) displaying artificially restored magnetosome chains localized at the positive curvature. Red line: projection of the geodetic axis in 2D space. Scale bars: 500 nm).

(c) A Δ*mamJ* cell with clustered magnetosomes. Scale bars: 500 nm.

(d) Several Δ*mamJ* cells transformed with the Nanotrap-to-K (mCherry-MamK and MamC-MBN) displaying artificially restored magnetosome chains localized at the positive curvature. Red line: projection of the geodetic axis in 2D space. Scale bars: 1 μm (insets: 500 nm).

(e) The *mamJY* double mutant contains clustered magnetosomes due to the dominant Δ *mamJ* phenotype. Scale bar: 500 nm.

(f) Δ*mamJY* cells transformed with the Nanotrap-to-K harbor synthetically restored magnetosome chains localized at the positive curvature. Red line: projection of the geodetic axis in 2D. Scale bars: 500 nm. Similar magnetosome localization patterns were observed in cells from three experiments using independent mutant strains and cell preparations.

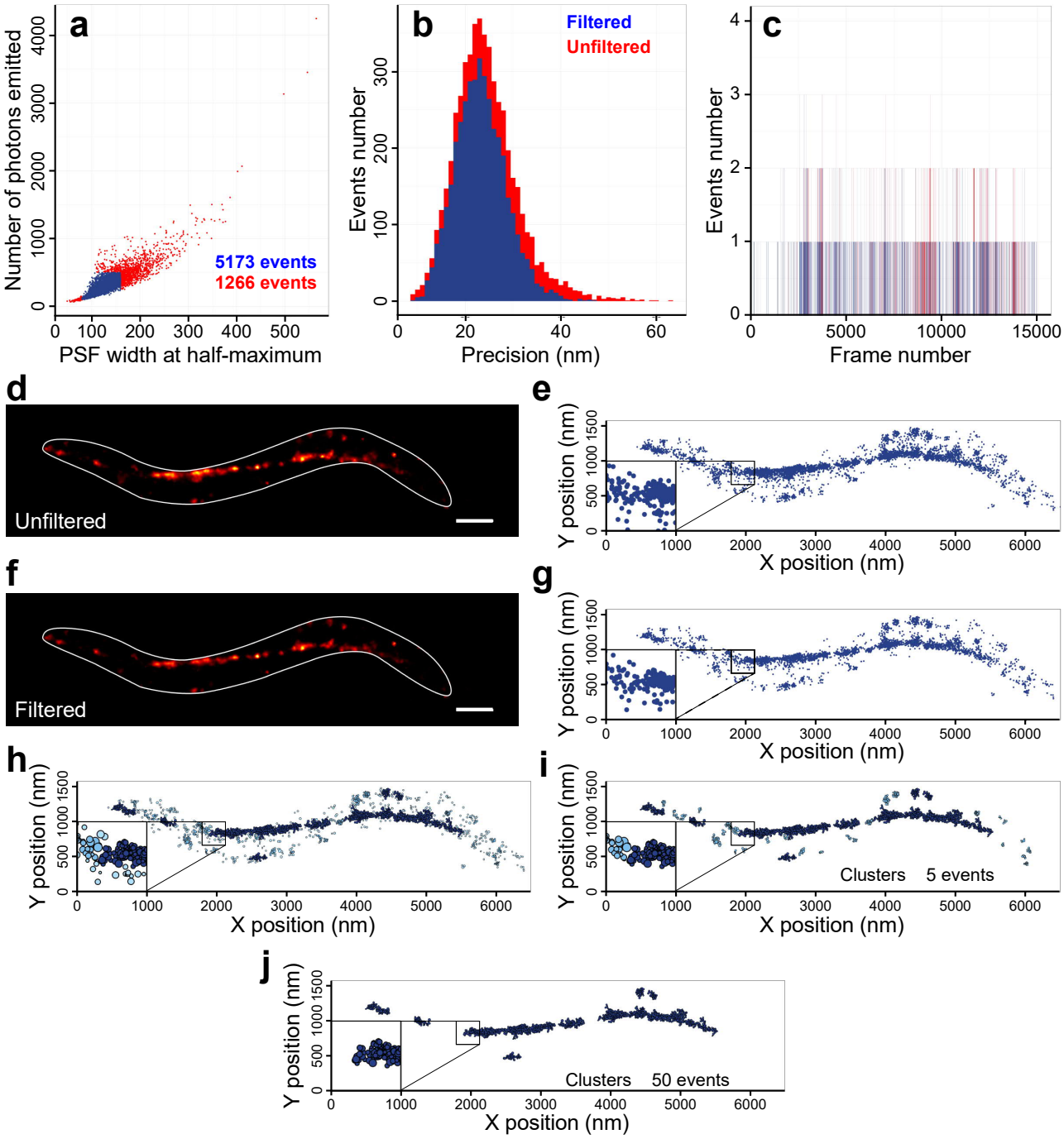

Supplementary Figure 12. PALM imaging quality assurance: data filtering and details

Filtering parameters are: PSF FWHM (80 - 160 nm), fluorophore emitted photon number (100 - 500). To show an example of the filtering effects and quality of the PALM imaging, a selected single cell is shown (Δ*mamK* plus Dendra2-MamY).

(a) Plot of PSF width at half-maximum versus number of emitted photons.

(b) Plot of localization precision area versus number of events.

(c) Number of events per frame for a single cell.

(d-g) PSF rendering and centroids localization of the **(d-e)** pre-filtered and **(f-g)** post-filtered cell. Scale bars: 500 nm. Results are representative of three independent experiments.

(h-j) Application of the clustering algorithm. **(h)** All clusters rendered, **(i)** clusters ≥5 molecules and **(j)** ≥50 molecules. Cluster color code: light blue, clusters <5 molecules; blue, clusters of 5 to 50 molecules; dark blue, clusters >50 molecules. Insets: magnification of the indicated area showing either the centroids or clusters of molecules rendered with their corresponding localization precision area.

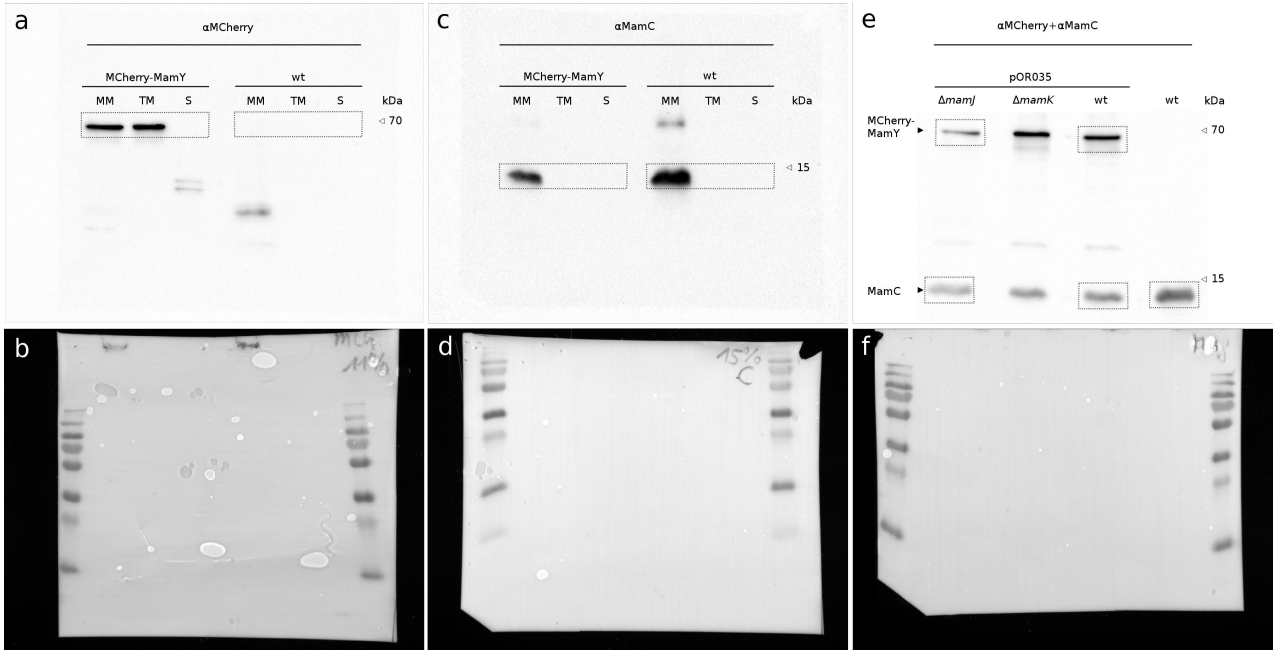

Supplementary Figure 13. Immunoblot raw data: full length blots.

(a-d) Related to Figure 3b of the manuscript.

(a) Immunodetection of mCherry-labelled MamY in fractionated lysates of cells containing pOR035 (lanes 1-3) and WT as control (lanes 4-6) by chemiluminescence. Lanes 1 and 4 were loaded with isolated magnetosomes (MM), lanes 2 and 5 with total membrane (TM) and lanes 3 and 6 with soluble fractions (S).

(b, d) Daylight exposure of the probed membranes.

(c) Second blot containing the same samples as in (a) but probed with αMamC antibody as control for cross-contamination of the fractionated cell lysates.

(e-f) Related to Supplementary Figure 5c of the manuscript and show the result of simultaneous detection of mCherry (fused to MamY) and MamC in purified magnetosomes from the indicated strains. The second lane (Δ*mamK*) is not shown and not mentioned in the main text.

The dashed boxes indicate the membrane sections shown in the main or supplementary figure, respectively. The size standard used was PageRuler Plus Prestained Protein Ladder (Thermo Scientific). Similar results were obtained in at least two independent experiments.

Supplementary Notes

MamY must be present at the cytoplasmic membrane to localize magnetosomes properly

Since we found MamY highly enriched in the cellular and the magnetosome membrane, we examined whether the presence of MamY on the magnetosome surface alone is sufficient to guide magnetosomes towards the geodetic axis. To this end, we used the Δ*mamY* strain to chromosomally express a chimeric MamC-MamY$_{CD}$ fusion, where MamC substituted the MamY TM domain and served as highly magnetosome-specific membrane anchor. TEM micrographs of this strain showed agglomerated magnetosomes mislocalized mostly at the negative curvature (Supplementary Fig. 5a). It has to be noted that in this strain, *mamC-mamY*$_{CD}$ is the only source of *mamY*, and the clustering of magnetosomes occurred in the presence of the MC-organizing proteins MamJ and MamK, suggesting that MamY may interact (directly or indirectly) via its C-terminus with MamJ (or MamY) located on the nearest neighboring magnetosome. Therefore, MamC-MamY$_{CD}$ did not complement the function of the native MamY. Expression of *mamC-mamY*$_{CD}$ in WT cells (native *mamY* present) induced magnetosomes clustering as well, indicating a negative dominant effect; however, magnetosomes localized properly at the positive curvature likely due to the influence of native MamY (Supplementary Fig. 5b). This suggests that MamY needs to be present at the cytoplasmic membrane to convey the MC to the geodetic position.

The cytoplasmic domain of MamY forms high oligomeric structures *in vitro*

To corroborate the assumed self-interaction and polymerization properties of MamY, we analyzed its intermolecular interaction capability *in vitro* using dynamic light scattering (DLS). To this end, we purified the cytoplasmic domain of MamY (MamY$_{CD}$) and tested for polymerization under different pH. DLS analysis in phosphate buffer at pH 7.4 resulted in one prominent peak for particles with a hydrodynamic radius of approximately 3 nm (Supplementary Fig. 9a, black line), ranging from 2 to 5 nm, and equivalent to 90.2% of total molecules mass. Given that purified MamY$_{CD}$ has a theoretical molecular weight of ~34 kDa and that a hydrodynamic radius of 3 nm is equivalent to about 44 kDa (2 to 5 nm represent ~18 and ~140 kDa, respectively), it can be hypothesized that this species may be composed of monomers, dimers and small (few molecules) oligomers of MamY$_{CD}$. In addition, a minor group of larger species with a radius between

10 and 84 nm (9.8% of the mass) could be observed (Supplementary Fig. 9a, black line). When the pH was increased to 8.0 (Supplementary Fig. 9a, red line), the proportion of larger sized particles (10 to 84 nm) rose to 54.4% of the total mass. The most abundant species of these large sized particles displayed radius sizes between 10 to 20 nm, which corresponds to an estimated range between 760 to 3,700 kDa (85 nm particles are ~110,000 kDa). However, lowering the pH from 8.0 to 6.0 resulted in loss of the large species and enrichment of the smaller sized particles <10 nm, the latter representing 92.7% of the total mass (Supplementary Fig. 9a, blue line), similar to the initial value at pH 7.4 (90.2% Supplementary Fig. 9a, black line). This suggests that the MamY cytoplasmic domain is capable to assemble into higher order oligomeric structures in solution, and that this behavior is pH dependent.

In a second set of experiments, we tested whether this polymerization is reproducible under conditions closer to physiological pH, i.e., upon more subtle pH shifts around 7.4. We again started at pH 7.4 with 100% of the particles being <10 nm (Supplementary Fig. 9b, black line). Upon a slight increase in the pH to 7.6, we observed a complete conversion of the small-sized particles to particles with a hydrodynamic radius between 25 to 66 nm, which now represented 100% of the total mass (Supplementary Fig. 9b, red line). This demonstrates that the oligomerization can be triggered by slight pH shifts that could well take place locally under physiological conditions. Interestingly, decreasing the pH from 7.6 back to 7.4 was sufficient to disassemble the polymers almost completely and resulted in 99.4% of species <10 nm (Supplementary Fig. 9b, blue line), which is close to the starting proportion at pH 7.4 (Supplementary Fig. 9b, black line). A subsequent increase back to pH 7.6 reproducibly caused a 100% of particles to assemble above 25 nm and up to 66 nm (Supplementary Fig. 9b, green line). Thus, our results suggest that MamY oligomerization can be mediated by its cytoplasmic domain; controlled by pH changes within a physiological range and is fully reversible. Self-interaction capabilities of MamY $_{Full}$ and the truncated versions (MamY $_{TMD\text{-}CD(266)}$ and MamY$_{CD}$) were confirmed *in vivo* by BTH assay (Supplementary Fig. 5e), again indicating that MamY as other scaffolding proteins has the potential to form homo-oligomeric complexes *in vivo*.

Nearest neighbor distances analysis of MamY molecules by PALM support non-random distribution directed at the geodetic axis

To determine whether the observed distribution of MamY molecules diverges from a theoretical, independent distribution (i.e., randomly distributed data considering identical area and events per cell), we analyzed the distances among neighboring events. Nearest neighbor distances of the experimental data displayed a cumulative distribution with a hyperbolic behavior (Fig. 4e inset: black, green and red lines), where 50% (half-maximum) of the molecules had a neighboring molecule at a distance of < 6 nm (and 80% < 10 nm). The difference between experimental and theoretical data suggests that the MamY molecules have a strong tendency to be closer than expected for a random distribution (Fig. 4e inset, blue line). In conclusion, the nearest neighbor distances of events support the notion that the MamY molecules become enriched at specific areas of the cell membrane where they localize tightly and potentially interact.

Validation of clustering algorithm using the recognized filament-forming protein MamK

We validated our clustering algorithm pipeline using the well-characterized actin-like MamK protein for which filament formation by self-interaction and polymerization has been demonstrated unambiguously [1-6]. When we applied the clustering algorithm to the Dendra2-MamK PALM data set, we consistently identified MamK as a continuous filamentous structure (Supplementary Fig. 8a). Therefore, the MamK analysis endorsed our algorithm pipeline to accurately find clusters of interacting proteins based on proximity *in vivo* and also as suitable and effective tool to segment a polymeric structure in an unbiased and automated manner. Occasionally detected clusters that seemingly branch from the linear MamK (and MamY) structures are considered as artifacts that likely arise from the 2D imaging which generates a projection of the whole cell volume.

Supplementary Discussion

Magnetosome chain assembly in curved magnetotactic bacteria

Despite of overall similarity and close relation, the two most extensively investigated magnetotactic bacteria models, *Mgryph* and *Mmagnet*, have shown remarkable differences in magnetosome assembly and positioning. Firstly, *Mgryph* assembles a single, continuous and midcell positioned MC [7]. In contrast, *Mmagnet* forms many intra-chain vesicles that lack magnetite crystals, causing the MC to appear discontinuous or fragmented when examined by TEM [7-9]. Secondly, deletion of *mamK* in *Mgryph*[4] caused formation of shorter and fragmented MCs, while the isogenic mutant in *Mmagnet* displayed scattered magnetosomes[5]. Third, *mamJ* deletion in *Mgryph* caused the MC to collapse, resulting in clustered magnetosomes[10]. The *mamJ* deletion in *Mmagnet*, however, merely resulted in wider gaps within the chain [9], reminiscent of the *Mgryph mamK* mutant. Those differences are in part attributed to the presence of a "magnetosome islet" in the *Mmagnet* genome containing paralogs of magnetosome-related genes [9,11].

Now, deletion of *mamY* in *Mgryph* caused a MC mispositioning (displaced from the geodetic axis); while the corresponding mutation in *Mmagnet* resulted only in slightly enlarged magnetosome vesicles [12] whereas no evident impact on MC positioning was reported. However, such rather subtle phenotype may also have escaped detection. Nevertheless, *Mmagnet*-MamY has been observed as patches localizing at sites of inner positive curvature[12] or as linear structure transiting the cell from positive-to-positive inner curvatures in its native host[13], similar to the positioning of MamY in *Mgryph* and very likely corresponding to a geodetic path. Interestingly, heterologously expressed *Mmagnet*-MamY in *Mgryph* showed a geodetic positioning (Supplementary Fig. 4n, left panel), and this localization was even preserved in absence of native MamY and other magnetosome-related proteins (Supplementary Fig. 4n, right panel). Consistently, sequence homologs of MamY are found in all curved magnetotactic bacteria known to date but not in cocci or rod-shaped species. This suggests that the function of MamY including its curvature-sensitivity is conserved and tied to dedicated magnetosome positioning in curved magnetotactic bacteria.

Our results also point towards a vital role of MamJ, a protein so far known to be essential to connect magnetosomes to the actin-like MamK filaments [10,14] and to transduce forces from the dynamic filaments to the magnetosomes which is needed to generate a single midcell positioned MC in *Mgryph*[15]. We assume that,

in a similar manner, MamJ must also (indirectly) be involved in recruitment of the magnetosomes to the MamY structural element (Fig. 6b). Besides the very similar phenotype of the *mamJ* and *mamKY* deletion mutants, this notion is supported by three observations: (i) chains are missing in the *mamJ* mutant (i.e., even in presence of MamY), (ii) the function of MamJ can be replaced by a Nanotrap (where magnetosomes are synthetically tethered to MamY, Fig. 5) and (iii) reconstruction of a synthetic MC onto the MamK filament in the Δ*mamJ* strain leads to a single MC at midcell, but without geodetic positioning (Supplementary Fig. 11d). The notion that MamY forms a rigid cytoskeleton-like structure is supported by our observation that the linear assemblies did not disappear upon dramatic changes in cell shape by formation of spheroplasts.

Spatially restricted MamY interaction likely promotes geodetic positioning

We showed that MamY forms a stable continuous and linear structure along the inner positively curved membrane, thereby identifying the geodetic axis where it recruits and tethers the MC, i.e., the magnetoreceptor. But, how does MamY itself become precisely positioned at the geodetic axis? Since single proteins are far too small to sense topologies of the cytoplasmic membrane [16], a first indispensable prerequisite is a certain level of homo-oligomerization and/or polymerization to form an extended structure. Based on our DLS, BTH and PALM results, we propose that MamY mainly exists in membrane-bound oligomeric clusters. Oligomerization occurs locally and stochastic *ab initio* presumably through interaction of the cytoplasmic domains (Fig. 4g) and seemingly modulated in a pH-dependent manner. Although the mode of this interaction at submolecular resolution remains to be unrevealed, there are well-characterized examples for proteins that oligomerize by conformational changes upon pH shifts. This type of oligomerization is known as 3D domain swapping and mediated by interchange of corresponding protein domains between a variable number of monomers enabling formation of dimers, oligomers or polymers [17-21]. It is reasonable to hypothesize that MamY monomers polymerize by 3D domain swapping as well, e.g. by interchanging cytoplasmic domain segments among amino acids 85 to 266. Thereby, the soluble MamY $_{CD}$ could assemble into rather flexible open-ended oligomers (Fig. 6c), likely corresponding to the species of larger particles observed *in vitro* by DLS upon slight pH shifts and to the dense molecule clusters seen by PALM *in vivo*. However, the full-length protein (including the TM domain) carries an additional anchor

point at each molecule, which (i) limits molecule diffusion to two dimensions and (ii) constrains the orientation by which a monomer is added to a complex at the membrane. Such defined positioning could well stabilize additional lateral intermolecular interactions and promote growth of oligomeric patches as seen by 3D-SIM and PALM. Larger clusters or patches could become sensitive to membrane curvature and gradually enrich at the inner positive curvature, which, in turn, would cause local crowding and promote further inter-oligomer interactions due to proximity and result in a linearly extended sheet-like assembly (Fig. 6d). This higher-order structure composed of MamY molecules organized in a single plane then likely grows large enough to localize exclusively to a continuous stretch of positive membrane curvature ultimately generating a cell-spanning rigid polymeric structure along the geodetic spirillum axis (Fig. 6a and 6d). Similar considerations have been made for DivIVA, a membrane-associated negative curvature-sensing protein[16]. However, thus far, it cannot be fully excluded that the MamY curvature sensing capability may also be indirect and mediated by an unknown interacting factor. Yet, such a factor would need to be present in both *Mgryph* and *R. rubrum.* Besides an elusive interacting protein, a significant contribution to MamY localization could well be provided by a deviant membrane lipid composition along the positive curvature similar as known for negative membranes such as cell poles or constriction sites [22-25]. Finally, an association with a conserved periplasmic structure is also conceivable.

Functional domains, structurally and functionally related proteins

Since the N-terminal TM domain together with a segment of the cytoplasmic domain (MamY $_{TMD\text{-}CD(266)}$) are likely essential for generation of the MamY linear structure and for curvature sensing (supported by the observed localization pattern in the heterologous host *R. rubrum*), we suggest that MamY can be divided into three functional domains: (i) The TM domain is essential to bind the protein to the cytoplasmic membrane and to restrict diffusion of the molecule to the inner cell surface. (ii) The central cytoplasmic α-helical part, which seems essential for self-interaction likely by domain swap. Both domains together mediate spatial orientation of the molecule and complex-formation as prerequisite for curvature sensing. (iii) The C-terminus is dispensable for this function but responsible for recruitment of the magnetosome chain to the identified geodetic path.

Interestingly, there are examples of eukaryotic cytoskeleton-associated proteins that are involved in support and positioning of the actin cytoskeleton at, e.g., focal adhesion plaques. Some of them undergo 3D domain swapping, such as the Focal Adhesion Kinase (involved in actin network plasticity) and Vinculin (a structural protein that tethers actin to the membrane) [20,21]. Remarkably, a recent *de novo* modeling of MamY described its cytosolic domain as intertwisted α-helices and having high structural similarity to Talin [26], an eukaryotic Integrin-associated protein positioned at focal adhesion plaques, where it functions to integrate and mechanically support microtubules, actin filaments and organelles [27]. Moreover, *in silico* examination of MamY from the closely related *Mmagnet* suggests similarity to eukaryotic bin/amphiphysin/rvs (BAR) domains [12], able to sense and induce membrane sections with positive curvature [28]. Hence, despite the lack of sequence homologs, MamY appears (i) structurally (tertiary structure) (ii) mechanistically (self-interaction mode) and (iii) functionally (organelle organization and topology sensing) related to eukaryotic cytoskeletal counterparts.

In a similar example, eukaryotic actin and the bacterial actin-like MreB exhibit low conservation on primary sequence level, but share strong structural (3D fold) [29,30] and functional (as cytoskeletal elements) similarity. Therefore, we speculate that MamY may represent a bacterial functional homolog of eukaryotic cytoskeletal proteins although structural examination of MamY at atomic resolution must unambiguously sustain this postulation.

Supplementary Videos Legend

Supplementary Video 1. Cryo-ET and 3D-rendering of a WT cell (mpg, 45 MB)
Cryo-electron tomography of a WT cell. View through the z-stack tomogram of the cell at 22,500× magnification. Magnetite crystals: red; magnetosome membrane vesicles: yellow; MamK filament: green; inner and outer cellular membrane: blue. This movie is related to Fig. 1c-e, and is representative of three independent experiments.

Supplementary Video 2. Cryo-ET and 3D-rendering of a Δ*mamY* cell (mpg, 41 MB)
Cryo-electron tomography of a Δ*mamY* cell. View through the z-stack tomogram of the cell at 22,500× magnification. Magnetite crystals: red; magnetosome membrane vesicles: yellow; MamK filament: green; inner and outer cellular membrane: blue. This movie is related to Fig. 1g-j, and is representative of three independent experiments.

Supplementary Video 3. 3D-SIM of mCherry-MamY (mp4, 31 KB)
Fluorescence signal of mCherry-MamY in an elongated *Mgryph* cell analyzed by 3D-SIM. The movie shows a 3D-rendering of the mCherry-MamY signal rotating in 360º first around the *x*-axis and subsequently around the *y*-axis, depicting how the MamY linear structure localizes along the positive curvature of the spirillum-shaped cell. This movie is related to Fig. 4a-c and is representative of two independent experiments.

Supplementary Tables

Table 1. Bacterial strains created and used in this work

Strain*	Genotype or characteristics	Reference or source
M. gryphiswaldense		
M. gryph WT	Wild-type MSR-1 R3/S1 (Rif^R, Sm^R).	Schultheiss and Schüler, 2003 [31]
Δ*mamJ*	Δ*mamJ*	Scheffel et al, 2006 [10]
Δ*mamK*	Δ*mamK*	Katzmann et al, 2010 [4]
M. gryph -1B	Spontaneous non-magnetic mutant	Schübbe et al, 2003 [32]
FM019	*mamC-mCherry*	Raschdorf et al, 2014 [33]
FM021	*mamC-egfp*	Raschdorf et al, 2014 [33]
ΔMAI	*non-magnetic by deletion of the magnetosome island*	T. Zwiener, unpublished
MT001	Δ*mamY*	This work
MT002	Δ*mamJK*	Toro-Nahuelpan et al, 2016 [15]
MT015	Δ*mamKY*	This work
MT004	Δ*mamJY*	This work
FM52	*mCherry-mamY*	This work
FM53	*mCherry-mamY, mamC-egfp*	This work
FM71	*mCherry-mamY*$_{TMD-CD(266)}$	This work
FM55	*mamC-mamY*$_{CD}$	This work
FM56	*mamC-mamY*$_{CD}$, Δ*mamY*	This work
MT016	Δ*mamY*, conjugated with pMT099, Km^R	This work
MT017	Δ*mamKY*, conjugated with pMT099, Km^R	This work
MT018	Δ*mamKY*, conjugated with pMT0105, Km^R	This work
MT019	Δ*mamKY*, conjugated with pMT0106, Km^R	This work
MT020	Δ*mamJ*, conjugated with pMT104, Km^R	This work
MT021	Δ*mamJK*, conjugated with pMT104, Km^R	This work
MT022	Δ*mamY*, conjugated with pMT103, Km^R	This work
MT023	Δ*mamKY*, conjugated with pMT103, Km^R	This work
eMT016	*M. gryph* WT, conjugated with pOR035, Km^R	This work
eMT017	Δ*mamY*, conjugated with pOR035, Km^R	This work
eMT018	*M. gryph* WT, conjugated with pMT102, Km^R	This work
eMT019	Δ*mamK*, conjugated with pMT102, Km^R	This work
eMT020	*M. gryph* WT, conjugated with pMT062, Km^R	This work
eMT021	Δ*mamJ*, conjugated with pSB005, Km^R	This work
eMT022	Δ*mamJY*, conjugated with pSB005, Km^R	This work
eFM001	*M. gryph* WT, conjugated with pFM269, Km^R	This work
eFM002	*M. gryph* WT, conjugated with pFM269a, Km^R	This work
eFM003	*M. gryph* WT, conjugated with pFM269c, Km^R	This work
eFM004	*M. gryph* WT, conjugated with pFM269d, Km^R	This work
eFM005	*M. gryph* WT, conjugated with pFM269g, Km^R	This work
eFM006	FM019, conjugated with pFM269h, Km^R	This work
eFM007	Δ*mamY*, conjugated with pFM269, Km^R	This work
eFM008	Δ*mamY*, conjugated with pFM269a, Km^R	This work
eFM009	Δ*mamY*, conjugated with pFM269c, Km^R	This work
eFM010	Δ*mamY*, conjugated with pFM269d, Km^R	This work
eFM011	Δ*mamY*, conjugated with pFM269g, Km^R	This work
eFM012	*M. gryph* -1B, conjugated with pFM269, Km^R	This work
eFM013	*M. gryph* -1B, conjugated with pFM269a, Km^R	This work
eFM014	*M. gryph* -1B, conjugated with pFM269c, Km^R	This work
eFM015	*M. gryph* -1B, conjugated with pFM269d, Km^R	This work
eFM016	*M. gryph* -1B, conjugated with pFM269g, Km^R	This work
eFM017	*M. gryph* -1B, conjugated with pFM269h, Km^R	This work
eFM018	*M. gryph* WT, conjugated with pFM283, Km^R	This work
eFM019	ΔMAI, conjugated with pFM269 Km^R	This work
eFM020	ΔMAI, conjugated with pFM269j, Km^R	This work
eFM021	Δ*mamKY*, conjugated with pFM269c, Km^R	This work
eFM022	Δ*mamKY*, conjugated with pFM269h, Km^R	This work
eFM023	*M. gryph* WT, conjugated with pFM269j, Km^R	This work
R. rubrum		
R. rubrum	*R. rubrum* ATCC 11170 - WT	DSM467
eFM024	*R. rubrum*, conjugated with pFM269, Km^R	This work
eFM025	*R. rubrum*, conjugated with pFM269g, Km^R	This work
eFM026	*R. rubrum*, conjugated with pFM269h, Km^R	This work
E. coli		
DH5α	Host for cloning. F^- φ80*lac*ZΔM15 Δ(*lac*ZYA-*arg*F) U169 *rec*A1 *end*A1 *hsd*R17 (rK-, mK+) *pho*A *sup*E44 λ-*thi*-1 *gyr*A96 *rel*A1	Invitrogen
BW29427	Host for cloning and conjugation. *thrB1004 pro thi rpsL hsdS lacZ*ΔM15 *RP4-1360* Δ(*araBAD*)*567* Δ*dapA1341*::[*erm pir* (*wt*)]	Datsenko and Wanner (unpublished)
WM3064	Host for cloning and conjugation. *thrB1004 pro thi rpsL hsdS lacZ*ΔM15 *RP4-1360* Δ(*araBAD*)*567* Δ*dapA1341*::[*erm pir* (*wt*)]	W. Metcalf, (unpublished)
BTH101	Reporter strain for BTH assay (*cya*). F^- *cya-99 araD139 galE15 galK16 rpsL1 (Str^r) hsdR2 mcrA1 mcrB1*	Euromedex

*MT and FM strains are chromosomally stably modified. eMT and eFM strains: transformed with an episomal (replicative) vector.

Table 2. Plasmids created and used in this study

Plasmid	Relevant characteristics / purpose	Reference or source
pORFM-GalK-MCS	Integrative backbone vector for in-frame gene deletion. *ori*T, P_{tet}-galK, Km^R, Tc^R	Raschdorf et al, 2014 [33]
pBBR1-MCS2	Replicative backbone vector for *in trans* gene expression in *M. gryph*. *ori*T, mob, Km^R	Kovach et al, 1994 [34]
pMT009	pBBR1-MCS2 based vector. P_{mamAB}-*mCherry-mamK*; Km^R	Toro-Nahuelpan et al, 2016 [15]
pMT065	pBBR-MCS2, P_{tet}-*dendra2-mamK,* terminator-fragment, P_{Neo}-TetR; Km^R	Toro-Nahuelpan et al, 2016 [15]
pJH2	pBAM1 *ori*R6K, with P_{tet}-*mamC-magegfp*, terminator, P_{Neo}-TetR; Km^R, Ap^R	Borg et al, 2014 [35]
pMT062	pMT009 derivative, P_{mamAB}-*dendra2-mamK*	Toro-Nahuelpan et al, 2016 [15]
pFM237	pORFM-GalK derivative for *mamC-mCherry* chromosomal fusion	Raschdorf et al, 2014 [33]
pMT005	pORFM-GalK derivative, for *mamY* deletion	This work
pMT099	pJH2 derivative, P_{tet}-*mamY*	This work
pMT102	pMT065 derivative, P_{tet}-*dendra2-mamY*	This work
pMT104	pJH2 derivative, P_{tet}-*mamC-RBP_mamY-mCherry*	This work
pMT105	pMT099 derivative, P_{tet}-*mamK*	This work
pMT106	pMT099 derivative, P_{tet}-*mamK_mamY*	This work
pFM251	pORFM-GalK derivative harboring *mamC-*$mamY_{CD}$, for *mamC* replacement	This work
pFM252	pORFM-GalK derivative harboring *mamY-mCherry*	This work
pFM253	pORFM-GalK derivative harboring *mCherry*, for *mamY* upstream insertion, generating *mCherry-mamY*	This work
pFM269	pAP160 derivative, P_{tet}-$mamY_{Full}$-*egfp*	This work
pFM269a	pFM269 derivative, P_{tet}-$mamY_{TMD}$-*egfp*	This work
pFM269c	pFM269 derivative, P_{tet}-$mamY_{CD}$-*egfp*	This work
pFM269d	pFM269 derivative, P_{tet}-$mamY_{CD(301-371)}$-*egfp*	This work
pFM269g	pFM269 derivative, P_{tet}-$mamY_{TMD-CD(266)}$-*egfp*	This work
pFM269h	pFM269 derivative, P_{tet}-HK_{TM}-$mamY_{CD}$-*egfp*	This work
pFM269j	pFM269 derivative, , P_{tet}-*M. magnet -*$mamY_{Full}$-*egfp*	This work
pFM272	pORFM-GalK derivative harboring $mamY_{TMD-CD(266)}$, for chromosomal *mamY* replacement by *mCherry-mamY*, generating *mCherry-*$mamY_{TMD-CD(266)}$	This work
pFM283	pFM269 derivative, P_{tet}-HK_{TM}-*egfp*	This work
pFM269c-1	P_{tet}-*dendra2-*$mamY_{CD}$	This work
pFM269h-1	P_{tet}-*dendra2-*HK_{TM}-$mamY_{CD}$	This work
pET-MamY	Heterologous expression of $mamY_{CD}$	Invitrogen / this work
pSB005	pBBR1 derivative, P_{mamDC}-*mamC-RBP*, P_{mamAB}-*mCherry-mamK*, Km^R	This work
pOR035	pBBR1 derivative, P_{mamXY}-*mamY-mCherry*	This work

Table 3. DNA Oligonucleotides used in this study

Name	Sequence 5'→3'	Remarks
oMTN025	agacta**GTCGAC**CGCATC***T***CACTTTACTGACTGTGCATCGACGATTG	Overhang, ***Sal*I, *G to T exchange*** (introducing stop codon)
oMTN026	agatgggggtgacaaagttcATCAACATAAGGGCTGCTCCCGTG	Lowercases: complementary to oMTN027
oMTN027	gaactttgtcacccccatctCCGATGCGTGACGAAAGC	Lowercases: complementary to oMTN026
oMTN028	agacta**GCGGCCGC** GCTCATGGCGTAATCCAGCCCGGCG	Overhang, ***Not*I**
oMTN040	agacta**CATATG**AGTGAAGGTGAAGGCCAGGCC	Overhang, ***Nde*I**
oMTN310	agacta**CATATG**TTGATGAACTTTGTCAACAATGTATCAAAGACG	Overhang, ***Nde*I**
oMTN311	agacta**GCTAGC**ATGTTGATGAACTTTGTCAACAATGTATCAAAGACG	Overhang, ***Nhe*I**
oMTN312	agacta**TCTAGA**CTACGCATCGGAGATGGGGGTTC	Overhang, ***Xba*I**
oMTN324	agacta**CATATG**GCGATTGCGGCCATCATGGG	Overhang, ***Nde*I**
oMTN325	agacta**GGATCC**TCAGTCCATGCCGGAATCGGGC	Overhang, ***Bam*HI**
oMTN328	gacta**CATATG**AGCTTTCAACTTGCGCCGTACTTGGC	Overhang, ***Nde*I**
oMTN329	cgctgttgtccttaattcaagggtcagCTAGCTGGAGACGGTGACCTGGG	Lowercases: complementary to oMTN330
oMTN330	ctgacccttgaattaaggacaacagcgATGTTGATGAACTTTGTCAACAATGTATCAAAGACG ATTAAC	Lowercases: complementary to oMTN329
oMTN331	gacta**TCTAGA**TTACTTGTACAGCTCGTCCATGCCGCC	Overhang, ***Xba*I**
oMTN345	cgagcccgagcccgaGGCCAATTCTTCCCTCAGAATGTCTTCGTC	Lowercases: complementary to oMTN346
oMTN346	tcgggctcgggctcgGGC	Lowercases: complementary to oMTN345
oMTN053	agacta**TCTAGA**TCACTGACCGGAAACGTCACCAAGCTG	Overhang, ***Xba*I**
oFM435	agacta**GGTACC**AGAACCGTCGAGAGCGTGAAGTCTGAAATTTCC	Overhang, ***Kpn*I**
oFM436	agacta**GAATTC**TTATCACGCATCGGAGATGGGGGTTCC	Overhang, ***Eco*RI**
oFM439	agacta**GTCGAC**GCTTTCAGTGGCTGGAATAATATTTTCTCAATGCTCC	Overhang, ***Sal*I**
oFM440	agacta**ACTAGTCCCGGG** CGCATCGGAGATGGGGGTTCCATCG	Overhang, ***Spe*I, *Xma*I**
oFM441	agacta**CCCGGG**GGTACCTTAAGATCTCGAGCTCCGGAGAATTCGGCGGCCGCG GATCCT ATGAGCAAGGGCGAGGAGGATAACATGG	Overhang, ***Xma*I**
oFM442	ctttcgtcacctaggcttGTACAGCTCGTCCATGC	Lowercases: complementary to oFM443
oFM443	aagcctaggtgacgaaagCCGACGTCCGAAATTGCATGG	Lowercases: complementary to oFM442
oFM444	agacta**ACTAGT**GAGCGAAGTCAGCCGGTGTCGTGC	Overhang, ***Spe*I**
oFM446	agacta**GTCGAC** CGCCTATGCTCTGCTCAACTCTCCAG	Overhang, ***Sal*I**
oFM447	cttgctcatcataagggcTGCTCCCGTGGTGG	Lowercases: complementary to oFM448
oFM448	gcccttatgatgagcaagGGCGAGGAGGATAACATGG	Lowercases: complementary to oFM447
oFM449	agacta**GGATCCGCGGCCGCC** GAATTC	Overhang, ***Bam*HI, *Not*I**
oFM450	agacta**GCGGCCGCGGATCC** AATGTTGATGAACTTTGTCAACAATGTATCAAAG ACGATTAACGG	Overhang, ***Not*I, *Bam*HI**
oFM451	agacta**ACTAGT**CGCAGGATTTTGGAAATCTGCTGGCGC	Overhang, ***Spe*I**
oFM482	agacta**CATATG**GTGGCCGACCGGTGACGCGTAACGTTCGCTAGCAGACTTCACG CTCTCGACGGTTCTCAC	Overhang, ***Nde*I**
oFM483a	agacta**CATATG**GTGGCCGACCGGTGACGCGTAACGTTCGCTAGCGTCGCCATGG GCCGCGTTCAGG	Overhang, ***Nde*I**
oFM484	tagacta**AAGCTT**AGGAGATCAGCTTATGTTGATGAACTTTGTCAACAATGTATCA AAGACGATTAACGG	Overhang, ***Hind*III**
oFM485	tagacta**AAGCTT**AGGAGATCAGCTTATGGAAATTTCCACCCTGTCCCAGCGGG	Overhang, ***Hind*III**
oFM486	tagacta**AAGCTT**AGGAGATCAGCTTATGCAATTGCAGCAATGCGCGATTGGTGC C	Overhang, ***Hind*III**
oFM487	agacta**CATATG**GTGGCCGACCGGTGACGCGTAACGTTCGCTAGCCGCATCGGA GATGGGGGTTCCATCG	Overhang, ***Nde*I**
oFM514	agacta**CCTAGG**GTCGGAATGGTTGACGACCTCGCTG	Overhang, **AvrII**
oFM556	agacta**AAGCTT**AGGAGATCAGCTTATGAGCGCAATTGCCCCTTATTCCCTGAG	Overhang, ***Hind*III**
oFM557	gacggtcagcttggtgatCAACGTGG	Lowercases: complementary to oFM558
oFM558	atcaccaagctgaccgtcGAAATTTCCACCCTGTCCCAGCGGG	Lowercases: complementary to oFM557
oFM560	agacta**CATATG**AGCGCAATTGCCCCTTATTCCCTGAG	Overhang, ***Nde*I**
oFM561	agacta**CATATG**GTGGCCGACCGGTGACGCGTAACGTTCGCTAGCACCTGACGGC GTCGGCGCC	Overhang, ***Nde*I**
oFM564	agacta**CATATG**ATGAGTGAAGGTGAAGGCCAGGCCAAG	Overhang, ***Nde*I**
oFM565	gtggtcgcattatcactgACCGGAAACGTCACCAAGCTG	Lowercases: complementary to oFM566
oFM566	cagtgataatgcgaccacCACAGCCACCACG	Lowercases: complementary to oFM565
oFM567	agacta**TCTAGA**TCATTACGCATCGGAGATGGGGGTTCCATCG	Overhang, ***Xba*I**
BTH_Yf1	agacta**CTGCAG**GATGTTGATGAACTTTGTCAACAATGTATCAAAGACGATTAAC GG	Overhang, ***Pst*I**
BTH_Yf5	agacta**CTGCAG**GGATGTTGATGAACTTTGTCAACAATGTATCAAAGACGATTAA CGG	Overhang, ***Pst*I**
BTH_Yf9	agacta**CTGCAG**GGAAATTTCCACCCTGTCCCAGCGGG	Overhang, ***Pst*I**
BTH_Yf13	agacta**CTGCAG**GGGAAATTTCCACCCTGTCCCAGCGGG	Overhang, ***Pst*I**
BTH_Yr3	agacta**GAATTC**GACGCATCGGAGATGGGGGTTCC	Overhang, ***Eco*RI**
BTH_Yr4	agacta**GAATTC**GAGTCGCCATGGGCCGCGTTCAGG	Overhang, ***Eco*RI**
BTH_Yr5	agacta**GAATTC**TCACGCATCGGAGATGGGGGTTCC	Overhang, ***Eco*RI**
BTH_Yr6	agacta**GAATTC**TCAGTCGCCATGGGCCGCGTTCAGG	Overhang, ***Eco*RI**
oOR087	ATTA**GGATCC**GGCAGCCTCATTTAAACATTCAGG	Overhang, ***Bam*HI**
oOR088	TTAC**AAGCTTCATATG**GGCTGCTCCCGTGGTGG	Overhang, ***Hind*III**, ***Nde*I**
oOR089	ACTG**CATATG**TTGATGAACTTTGTCAACAATG	Overhang, ***Nde*I**
oOR090	ACTC**CTCGAG**TCA**GCTAGC**CGCATCGGAGATGGGG	Overhang, ***Xho*I**, ***Nhe*I**
oOR100	TCAC**GCTAGC**GAACGTTACGCGTCACCGG	Overhang, ***Nhe*I**
oOR101	ATCT**ATGCAT**TAGTCAATTGTTACTTGTACAGCTCGTCCATGC	Overhang, ***Nsi*I**

Supplementary References

1 Ozyamak, E., Kollman, J., Agard, D. A. & Komeili, A. The bacterial actin MamK: in vitro assembly behavior and filament architecture. *J Biol Chem* **288**, 4265-4277, doi:10.1074/jbc.M112.417030 (2013).

2 Bergeron, J. R. *et al.* Structure of the magnetosome-associated actin-like MamK filament at subnanometer resolution. *Protein Sci* **26**, 93-102, doi:10.1002/pro.2979 (2017).

3 Löwe, J., He, S., Scheres, S. H. & Savva, C. G. X-ray and cryo-EM structures of monomeric and filamentous actin-like protein MamK reveal changes associated with polymerization. *Proc Natl Acad Sci U S A* **113**, 13396-13401, doi:10.1073/pnas.1612034113 (2016).

4 Katzmann, E., Scheffel, A., Gruska, M., Plitzko, J. M. & Schüler, D. Loss of the actin-like protein MamK has pleiotropic effects on magnetosome formation and chain assembly in *Magnetospirillum gryphiswaldense*. *Mol Microbiol* **77**, 208-224, doi:10.1111/j.1365-2958.2010.07202.x (2010).

5 Komeili, A., Li, Z., Newman, D. & Jensen, G. Magnetosomes are cell membrane invaginations organized by the actin-like protein MamK. *Science* **311**, 242-245, doi:10.1126/science.1123231 (2006).

6 Sonkaria, S. *et al.* Insight into the assembly properties and functional organisation of the magnetotactic bacterial actin-like homolog, MamK. *PLoS One* **7**, e34189, doi:10.1371/journal.pone.0034189 (2012).

7 Uebe, R. & Schüler, D. Magnetosome biogenesis in magnetotactic bacteria. *Nat Rev Microbiol* **14**, 621-637, doi:10.1038/nrmicro.2016.99 (2016).

8 Komeili, A., Vali, H., Beveridge, T. & Newman, D. Magnetosome vesicles are present before magnetite formation, and MamA is required for their activation. *Proc Natl Acad Sci USA* **101**, 3839-3844, doi:10.1073/pnas.0400391101 (2004).

9 Draper, O. *et al.* MamK, a bacterial actin, forms dynamic filaments in vivo that are regulated by the acidic proteins MamJ and LimJ. *Mol Microbiol* **82**, 342-354, doi:10.1111/j.1365-2958.2011.07815.x (2011).

10 Scheffel, A. *et al.* An acidic protein aligns magnetosomes along a filamentous structure in magnetotactic bacteria. *Nature* **440**, 110-114, doi:10.1038/nature04382 (2006).

11 Rioux, J. B. *et al.* A second actin-like MamK protein in *Magnetospirillum magneticum* AMB-1 encoded outside the genomic magnetosome island. *PLoS One* **5**, e9151, doi:10.1371/journal.pone.0009151 (2010).

12 Tanaka, M., Arakaki, A. & Matsunaga, T. Identification and functional characterization of liposome tubulation protein from magnetotactic bacteria. *Molecular Microbiology* **76**, 480-488, doi:10.1111/j.1365-2958.2010.07117.x (2010).

13 Arakaki, A. *et al.* Comparative Subcellular Localization Analysis of Magnetosome Proteins Reveals a Unique Localization Behavior of Mms6 Protein onto Magnetite Crystals. *Journal of Bacteriology* **198**, 2794-2802, doi:10.1128/Jb.00280-16 (2016).

14 Scheffel, A. & Schüler, D. The acidic repetitive domain of the *Magnetospirillum gryphiswaldense* MamJ protein displays hypervariability but is not required for magnetosome chain assembly. *J Bacteriol* **189**, 6437-6446, doi:10.1128/JB.00421-07 (2007).

15 Toro-Nahuelpan, M. *et al.* Segregation of prokaryotic magnetosomes organelles is driven by treadmilling of a dynamic actin-like MamK filament. *BMC Biol* **14**, 88, doi:10.1186/s12915-016-0290-1 (2016).

16 Oliva, M. A. *et al.* Features critical for membrane binding revealed by DivIVA crystal structure. *EMBO J* **29**, 1988-2001, doi:10.1038/emboj.2010.99 (2010).

17 Bennett, M. J., Choe, S. & Eisenberg, D. Domain swapping: entangling alliances between proteins. *Proc Natl Acad Sci U S A* **91**, 3127-3131 (1994).

18 Janowski, R., Abrahamson, M., Grubb, A. & Jaskolski, M. Domain swapping in N-truncated human cystatin C. *J Mol Biol* **341**, 151-160, doi:10.1016/j.jmb.2004.06.013 (2004).

19 Yang, F. *et al.* Crystal structure of cyanovirin-N, a potent HIV-inactivating protein, shows unexpected domain swapping. *J Mol Biol* **288**, 403-412, doi:10.1006/jmbi.1999.2693 (1999).

20 Chinthalapudi, K., Rangarajan, E. S., Brown, D. T. & Izard, T. Differential lipid binding of vinculin isoforms promotes quasi-equivalent dimerization. *Proc Natl Acad Sci U S A* **113**, 9539-9544, doi:10.1073/pnas.1600702113 (2016).

21 Prutzman, K. C. *et al.* The focal adhesion targeting domain of focal adhesion kinase contains a hinge region that modulates tyrosine 926 phosphorylation. *Structure* **12**, 881-891, doi:10.1016/j.str.2004.02.028 (2004).

22 McMahon, H. T. & Boucrot, E. Membrane curvature at a glance. *J Cell Sci* **128**, 1065-1070, doi:10.1242/jcs.114454 (2015).

23 Kawai, F. *et al.* Cardiolipin domains in Bacillus subtilis marburg membranes. *J Bacteriol* **186**, 1475-1483 (2004).

24 Nishibori, A., Kusaka, J., Hara, H., Umeda, M. & Matsumoto, K. Phosphatidylethanolamine domains and localization of phospholipid synthases in Bacillus subtilis membranes. *J Bacteriol* **187**, 2163-2174, doi:10.1128/JB.187.6.2163-2174.2005 (2005).

25 Ramamurthi, K. S., Lecuyer, S., Stone, H. A. & Losick, R. Geometric Cue for Protein Localization in a Bacterium. *Science* **323**, 1354-1357, doi:10.1126/science.1169218 (2009).

26 Nudelman, H. & Zarivach, R. Structure prediction of magnetosome-associated proteins. *Front Microbiol* **5**, 9, doi:10.3389/fmicb.2014.00009 (2014).

27 Niggli, V., Kaufmann, S., Goldmann, W. H., Weber, T. & Isenberg, G. Identification of functional domains in the cytoskeletal protein talin. *Eur J Biochem* **224**, 951-957 (1994).

28 Peter, B. J. *et al.* BAR domains as sensors of membrane curvature: the amphiphysin BAR structure. *Science* **303**, 495-499, doi:10.1126/science.1092586 (2004).

29 Van den Ent, F., Amos, L. & Löwe, J. Prokaryotic origin of the actin cytoskeleton. *Nature* **413**, 39-44 (2001).

30 Holmes, K. C., Popp, D., Gebhard, W. & Kabsch, W. Atomic model of the actin filament. *Nature* **347**, 44-49, doi:10.1038/347044a0 (1990).

31 Schultheiss, D. & Schüler, D. Development of a genetic system for *Magnetospirillum gryphiswaldense*. *Archives of Microbiology* **179**, 89-94, doi:10.1007/s00203-002-0498-z (2003).

32 Schübbe, S. *et al.* Characterization of a Spontaneous Nonmagnetic Mutant of *Magnetospirillum gryphiswaldense* Reveals a Large Deletion Comprising a Putative Magnetosome Island. *J Bacteriol* **185**, 5779-5790, doi:10.1128/jb.185.19.5779-5790.2003 (2003).

33 Raschdorf, O., Plitzko, J. M., Schüler, D. & Müller, F. D. A tailored galK counterselection system for efficient markerless gene deletion and chromosomal tagging in *Magnetospirillum gryphiswaldense*. *Appl Environ Microbiol* **80**, 4323-4330, doi:10.1128/AEM.00588-14 (2014).

34 Kovach, M., Phillips, R., Elzer, P., Roop, R. & Peterson, K. pBBR1MCS: a broad-host-range cloning vector. *BioTechniques* **16**, 800-802. (1994).

35 Borg, S., Hofmann, J., Pollithy, A., Lang, C. & Schüler, D. New vectors for chromosomal integration enable high-level constitutive or inducible magnetosome expression of fusion proteins in *Magnetospirillum gryphiswaldense*. *Appl Environ Microbiol* **80**, 2609-2616, doi:10.1128/AEM.00192-14 (2014).